

A Review of the Terahertz Conductivity of Bulk and Nano-Materials

James Lloyd-Hughes · Tae-In Jeon

Received: 3 January 2012 / Accepted: 20 April 2012 /
Published online: 31 May 2012
© Springer Science+Business Media, LLC 2012

Abstract We review pioneering and recent studies of the conductivity of solid state systems at terahertz frequencies. A variety of theoretical formalisms that describe the terahertz conductivity of bulk, mesoscopic and nanoscale materials are outlined, and their validity and limitations are given. Experimental highlights are discussed from studies of inorganic semiconductors, organic materials (such as graphene, carbon nanotubes and polymers), metallic films and strongly correlated electron systems including superconductors.

Keywords Terahertz · Conductivity · Semiconductor · Superconductor

1 Introduction

The interaction of terahertz radiation with matter provides a vital low-energy probe of the electronic nature of a system close to its equilibrium state. Historically it has been challenging to generate and detect light in the far-infrared (or terahertz) range, roughly defined as 0.1–10 THz (or 0.4–40 meV), owing to the presence of background sources of incoherent light (room temperature is 25 meV, or 6 THz). The last two decades have seen a surge in interest

J. Lloyd-Hughes (✉)
Department of Physics, University of Oxford, Oxford, UK
e-mail: james.lloyd-hughes@physics.ox.ac.uk

T.-I. Jeon (✉)
Division of Electrical and Electronics Engineering,
Korea Maritime University, Busan, Korea
e-mail: jeon@hhu.ac.kr

in the generation, detection, and spectroscopic applications of THz radiation owing to rapid developments in both continuous wave systems and in pulsed sources based on terahertz time-domain spectroscopy (THz-TDS). Time-resolved techniques also offer novel experimental paradigms, such as tracking the dynamic photoconductivity of a material on picosecond to nanosecond timescales. The combination of dramatic improvements in experimental technique and its applicability to materials of contemporary interest is making the terahertz range an increasingly vital part of the electromagnetic spectrum.

There are a number of excellent reviews on terahertz spectroscopic techniques and applications. Ferguson and Zhang [1] discussed CW and pulsed THz systems and THz spectroscopy of biomolecules and semiconductors. Schmuttenmaer [2] reviewed methods of generating and detecting THz pulses, and discussed early applications of optical-pump terahertz-probe spectroscopy (OPTPS) in inorganic semiconductors and superconductors. Tonouchi [3] summarised the state-of-the-art for continuous wave and pulsed THz sources, and presented industrial and basic science applications. Baxter and Guglietta [4] discussed recent advances in spectrometer design, THz generation and detection, and chemical, biological and solid state applications. Jepsen *et al.* [5] provided an overview of photoconductive, non-linear and CW THz generation and detection, and reviewed industrial applications and the THz spectroscopy of organic molecules and aqueous solutions. Ulbricht *et al.* [6] detailed the technique of OPTPS and the transient photoconductivity of bulk and nanostructured semiconductors, in systems with and without quantum confinement. Nemec *et al.* [7] reviewed THz-TDS studies of polymer-fullerene heterojunctions and dye-sensitised nanoparticles. The dynamics of charges in superconductors and other correlated electron systems using THz-TDS and visible ultrafast spectroscopy has been reviewed by Averitt and Taylor [8] and more recently by Basov *et al.* [9]. Near-field THz imaging techniques were explained in depth by Adam [10].

In this article we review the equilibrium and photoconductivity at terahertz frequencies of bulk and nano-structured solid state materials, highlighting both pioneering early work and more recent discoveries. We provide a brief overview in Section 2 of THz-TDS systems. The definition of the complex conductivity is discussed in Section 2.1, and Section 2.2 describes how the complex conductivity can be obtained from experiment. Section 3 details the wide variety of THz conductivity models, starting with a time-domain examination of the Drude–Lorentz model’s limitations, including its breakdown when the electric field strength of the THz pulse is sufficiently high. Conductivity models valid for weakly localised and quantum confined carriers are then summarised. Subsequently we discuss THz conductivity studies of bulk and nanoscale inorganic semiconductors (Section 4), organic materials such as polymers, graphene and carbon nanotubes (Section 5), metallic thin films (Section 6) and correlated electron materials such as those that superconduct or exhibit colossal magnetoresistance (Section 7).

2 Complex conductivity: definition and experimental determination

In this review we report broadband spectroscopic studies typically obtained using THz-TDS, which measures the electric field of pulses of electromagnetic radiation directly in the time-domain. There are a number of reviews of this technique, as listed in the introduction, as a result of its widespread uptake over the last decade. We therefore summarise below the key components in a THz time-domain spectrometer, before discussing in Section 2.1 the definition of the complex conductivity. Subsequently, in Section 2.2 the validity of the expressions used to obtain the conductivity from experimental data is explored. Section 2.3 highlights the need for broadband measurements when the optical properties of a sample alter only slowly with frequency.

THz-TDS utilises short (<100 fs) pulses of infrared radiation (typically centred at 800 nm, from a mode-locked Ti:sapphire laser) to generate and detect single-cycle pulses of radiation. As the pulses have sub-picosecond duration they are broadband, with significant power from tens of GHz up to a few THz in typical setups. At high pulse fluences non-linear techniques such as difference frequency generation, optical rectification and gas plasma generation are efficient methods by which IR radiation can be downconverted into the THz range [11, 12]. With lower fluences photoconductive emitters are often employed, where a transient photocurrent generates a pulse of THz radiation [13, 14]. The photocurrent can arise from various fields that cause charge separation, such as an applied electric field (photoconductive switches, or Auston switches), surface accumulation or depletion fields [15, 16], and photo-Dember fields (created by a difference in the ballistic motion of an electron and a hole) [16, 17].

Two competing techniques are used to detect THz pulses coherently. In electro-optic sampling [18, 19] the electric field of the THz pulse changes the polarisation state of an IR gate pulse, which is often analysed by a Wollaston prism and balanced photodiodes. The electric field of the THz pulse can be directly calculated from the experimental signal using known parameters of the electro-optic crystal [20]. Given the importance of the THz electric field strength on establishing the validity of the Drude–Lorentz model of carrier transport (as discussed in Section 3.1), reporting the electric field strength of the THz pulse is vital. The photoconductive detection [14] of THz radiation pulses occurs by the inverse process to emission: a photocurrent created by a gate (detection) beam flows between two contacts under the influence of the THz electric field, producing a signal that is proportional to E_{THz} (when the material has a short photoconductivity decay time [21]).

A typical THz-TDS setup based on photoconductive antennae to generate and detect THz radiation is shown in Fig. 1. A burst of terahertz radiation is generated from the emitter chip when it is photoexcited by a subpicosecond laser pulse (with a few mW average beam power). The excited THz pulse is collimated by a silicon lens and propagates in free space before reflecting from

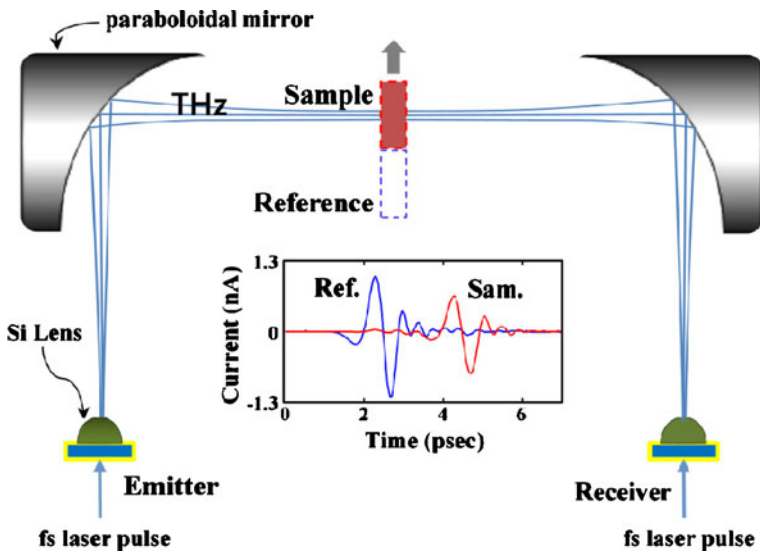


Fig. 1 A schematic diagram of a typical THz-TDS system. The *inset* shows a measured THz pulse for the reference scan (vacuum, *blue line*) and for a sample (*red line*).

a parabolic mirror. A second mirror reflects the THz pulse onto the detector, and the time-dependence of the THz pulse is obtained by scanning the relative time delay between the emitter excitation pulse and the detection pulse. A conductive sample is located between the two parabolic mirrors, and causes a time delay and a reduction in the magnitude of the THz pulse as shown in the figure's inset. The reference THz pulse can be measured without the sample. Using the magnitude and phase information of the spectra both the absorption and refractive index (and therefore σ) of the conducting sample can be determined, without resorting to the Kramers–Kronig relations.

THz-TDS has a number of advantages over incoherent techniques, such as

- the time-gated detection of THz pulses allows all spectrometer components to be at room temperature, by suppressing the incoherent background radiation;
- the ability to extract the complex optical properties of a material without use of the Kramers–Kronig relations;
- the possibility of removing Fabry–Perot reflections in thick substrates by windowing the time-domain data, which is not possible with incoherent techniques;
- the time-resolved photoconductivity on picosecond timescales can be accessed experimentally in a non-contact manner.

There are of course disadvantages of THz-TDS, such as the high cost of the technique (mainly due to the need for an ultrafast laser), and the frequency range of typical THz-TDS setups is not as broad as that of Fourier-

transform infrared spectrometers. In the terahertz range reflective optics (such as off-axis parabolic mirrors) are more desirable than dielectric components (such as lenses), and this is particularly true for THz-TDS where thin dielectric components can produce internal (Fabry–Perot) reflections that limit the useful experimental time range (and therefore the spectral resolution). One disadvantage of the phase-sensitivity of THz-TDS is apparent when the reflection geometry is used rather than the transmission geometry: the position of the reference mirror needs to be precisely determined to prevent phase errors entering into the calculated optical properties of the sample [22, 23]. Even in the transmission geometry care needs to be taken to not measure materials with absorbances that exceed the maximum value accessible by the spectrometer, as the calculated absorption coefficient can be incorrect if this is the case [24].

2.1 Definition of the complex conductivity

A variety of functions can be used to describe the response of a material to an electromagnetic wave. Fundamentally, the complex refractive index $\tilde{n} = n + i\kappa = \sqrt{\epsilon\mu}$ is the term that enters expressions for the transmission or reflectivity of a material, where the dielectric function (or permittivity) $\epsilon(\omega) = \epsilon_1(\omega) + i\epsilon_2(\omega)$ describes how easily an electric field penetrates the medium, and the permeability μ details the magnetic response. In this Review we will be primarily concerned with non-magnetic materials, for which $\mu = 1$. The dielectric function is in general complex, with a significant imaginary part ϵ_2 in spectral regions with absorption. It is often convenient to disentangle the contribution to ϵ from bound modes (lattice vibrations and core electrons) and the component arising from free charges. In the THz and mid-IR frequency ranges lattice vibrations contribute via transverse optical phonon absorption (in polar materials), while at optical frequencies interband transitions alter ϵ . Writing this lattice component as ϵ_L allows the following expression to be derived from Maxwell's equations

$$\epsilon(\omega) = \epsilon_L(\omega) + \frac{i\sigma(\omega)}{\omega\epsilon_0} \quad (1)$$

where ω is the angular frequency of the electromagnetic wave, and ϵ_0 is the permittivity of free space. The conductivity σ of mobile charges is also complex: $\sigma(\omega) = \sigma_1(\omega) + i\sigma_2(\omega)$. This expression is valid for a monochromatic plane wave propagating in the $\hat{\mathbf{k}}$ direction, with a time dependent electric field of the form $E(t) = E_0 e^{i(\mathbf{k}\cdot\mathbf{r} - \omega t)}$, which is the convention assumed throughout this review. With the opposite sign time dependence then $\sigma = \sigma_1 - i\sigma_2$.

In any study of the optical properties of a material it is vital to define in the constitutive relation for ϵ (Eq. 1) whether ϵ_L is a constant (such as the high-frequency or low-frequency dielectric constant ϵ_∞ , ϵ_s) or a function of frequency. If $\epsilon_L = \epsilon_\infty$ then the conductivity function

$$\sigma'(\omega) = \omega\epsilon_0(\epsilon(\omega) - \epsilon_\infty) \quad (2)$$

includes a contribution from the displacement of bound charges (such as TO phonons), and exhibits characteristic peaks in σ'_1 at the phonon frequencies. With $\epsilon_L(\omega)$ including the lattice response then

$$\sigma(\omega) = \omega\epsilon_0(\epsilon(\omega) - \epsilon_L(\omega)) \quad (3)$$

just represents the conductivity of mobile charges. To illustrate this, $\epsilon_1(\omega)$ is plotted in Fig. 2a for n-type GaAs, where the Drude–Lorentz conductivity (Section 3.1, Eq. 18) was used for σ in Eq. 1. In a polar semiconductor with a single TO-phonon mode ϵ_L is given by

$$\epsilon_L(\omega) = \epsilon_\infty + (\epsilon_s - \epsilon_\infty) \frac{\omega_{\text{TO}}^2}{\omega_{\text{TO}}^2 - \omega^2 - i\omega\Gamma}, \quad (4)$$

where ω_{TO} and Γ are the TO-phonon angular frequency and damping rate, and for GaAs the static dielectric constant $\epsilon_s = 12.95$, and at high frequencies $\epsilon_\infty = 10.89$. The influence of the TO phonon resonance on ϵ_1 can be seen in Fig. 2a near $\omega_{\text{TO}}/2\pi = 8.0$ THz, and appears as a peak in σ'_1 (dashed line in Fig. 2b) when $\epsilon_L(\omega) = \epsilon_s = 12.95$. In contrast the conductivity σ_1 of free electrons, given by the solid line, decreases monotonically with frequency. The negative ϵ_1 well below the plasma frequency (3.3 THz) is characteristic of metallic behaviour, where σ_1 is large.

While the choice of the function (\tilde{n} , σ , σ' , $1/\epsilon$, ϵ) to describe the optical response of a material is somewhat arbitrary, often the conductivity is preferred as it enables a straightforward consistency check if the dc conductivity is known. Theoretical models of the dynamical motion of charge carriers in materials are often described by the medium's conductivity. In addition, sum rules straightforwardly relate the integral of σ_1 over all frequencies to the free carrier density of the system. For instance, in a 3D system the electron density N is

$$N = \frac{2m^*}{\pi e^2} \int_0^\infty \sigma_1(\omega) d\omega. \quad (5)$$

where m^* is the electron effective mass. This sum rule allows the carrier density to be obtained provided that $\sigma_1(\omega)$ is measured over its entire range. The

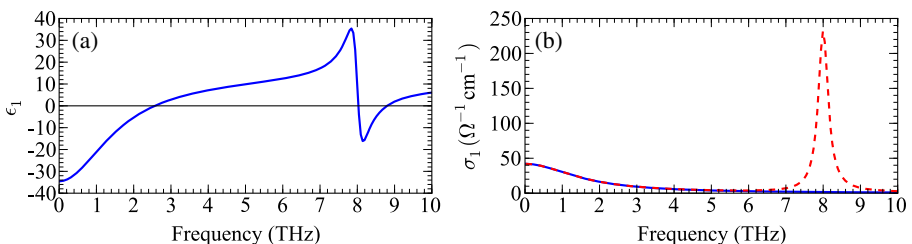


Fig. 2 **a** ϵ_1 for n-doped GaAs calculated from Eqs. 1, 4, and 18 ($N = 10^{17} \text{ cm}^{-3}$, $\tau = 100 \text{ fs}$, $\omega_{\text{TO}}/2\pi = 8.0 \text{ THz}$, $\Gamma = 2 \text{ THz}$). **b** σ_1 is shown just for free electrons (solid line, Eq. 3) and when the lattice contribution is included (dashed line, Eq. 3 with $\epsilon_L(\omega) = \epsilon_s = 12.95$).

conductivity σ can be calculated from \tilde{n} and ϵ_L using the following useful relations, which can be derived from Eq. 1

$$\sigma_1 = \omega\epsilon_0 (2n\kappa - \epsilon_{L,2}), \quad (6)$$

$$\sigma_2 = \omega\epsilon_0 (\epsilon_{L,1} - n^2 + \kappa^2). \quad (7)$$

2.2 Data analysis

In order to elucidate the methods by which the conductivity can be calculated from experimental data we consider the measured transmission through a uniform dielectric slab of thickness d and complex refractive index \tilde{n} , placed in free space. The transmission $T(\omega) = |T(\omega)|e^{i\phi(\omega)} = E_s(\omega)/E_r(\omega)$ is calculated from the Fourier-transform of the time-domain electric field E_s transmitted through the sample, and E_r for the reference (no sample). The transmission of this dielectric can be straightforwardly obtained from the Fresnel transmission (t_{ij}) and reflection (r_{ij}) coefficients, propagation factors of the form $\exp(i\tilde{n}\omega d/c)$, and a Fabry–Perot term F_{iji} describing reflections within the slab, giving

$$T(\omega) = t_{ij}t_{ji} \exp\left[i\frac{\omega d}{c}(\tilde{n}_j - \tilde{n}_i)\right] F_{iji}(\omega), \quad (8)$$

where the subscripts i and j denote free space and the sample, respectively. At normal incidence $t_{ij} = 2\tilde{n}_i/(\tilde{n}_i + \tilde{n}_j)$, $r_{ij} = (\tilde{n}_i - \tilde{n}_j)/(\tilde{n}_i + \tilde{n}_j)$, and

$$F_{iji}(\omega) = \sum_{p=0}^P \left[r_{ji}^2 \exp\left(i\frac{2\tilde{n}(\omega)\omega d}{c}\right) \right]^p, \quad (9)$$

where the upper limit P of the Fabry–Perot series is set by the number of internal reflections recorded in the time-domain data. For an arbitrary thickness d , one must calculate the complex transmission using a model for \tilde{n} , and compare it with experiment in order to extract the parameters entering \tilde{n} . Alternatively, methods exist to calculate \tilde{n} numerically [25]. However, for particular sample thicknesses Eq. 8 can be successfully inverted to obtain an analytic expression for \tilde{n} and thus $\sigma(\omega)$. The two limits of an exceedingly thick ($P = 0$) or thin ($P = \infty$) film yield expressions for \tilde{n} . Tackling first the thick film limit, as long as there is minimal absorption in the frequency range of interest then $\kappa \ll n$, allowing the Fresnel transmission coefficients to be approximated as real numbers. In that case the refractive index of the sample is just given by the phase of the complex transmission

$$n(\omega) = 1 + \frac{c}{\omega d} \phi(\omega), \quad (10)$$

and the absorption coefficient is

$$\alpha(\omega) = -\frac{2}{d} \ln \frac{|T(\omega)|}{|t_{ij}t_{ji}|}. \quad (11)$$

Considering now the thin film limit ($P = \infty$), the Fabry–Perot term becomes

$$\text{FP}_{\text{iji}} = \sum_{p=0}^{\infty} \left[r_{ij}^2 e^{2i\tilde{n}\omega\delta/c} \right]^p = \frac{1}{1 - r_{ij}^2 e^{2i\tilde{n}\omega\delta/c}}, \quad (12)$$

which allows the transmission to be written exactly as

$$T(\omega) = \frac{2\tilde{n}e^{-i\omega d/c}}{2\tilde{n}\cos(\tilde{n}\omega d/c) - i(\tilde{n}^2 + 1)\sin(\tilde{n}\omega d/c)}. \quad (13)$$

In order to be able to rearrange Eq. 13 for \tilde{n} the approximation of negligible optical thickness needs to be made. This can be written $n\omega d/c \ll 1$ and $\kappa\omega d/c \ll 1$, so that the approximations $\cos x \sim 1$, $\sin x \sim x$ and $e^{-x} = 1$ can be obtained by taking the first order Taylor series expansion of x . This yields:

$$T(\omega) = \frac{2}{2 - i(\tilde{n}^2 + 1)\omega d/c}, \quad (14)$$

which can be inverted to find $\epsilon = \tilde{n}^2$. Utilising Eq. 1 the conductivity of the sample is

$$\sigma(\omega) = \frac{2}{Z_0 d} \left(\frac{1}{T} - 1 \right) + i(\epsilon_L + 1)\omega\epsilon_0, \quad (15)$$

where the impedance of free space is $Z_0 = \sqrt{\mu_0/\epsilon_0}$. With the additional assumption of a highly conductive thin film, the further approximation $\tilde{n}^2 + 1 = \epsilon + 1 \sim i\sigma/\omega\epsilon_0$ can be made in Eq. 14, which removes the second term from Eq. 15. In this case the transmission is given just by

$$T(\omega) = \frac{2}{2 + i\sigma d Z_0}, \quad (16)$$

which is the expression for the transmission of a thin conductive film first applied to superconductors by Glover and Tinkham [26].

If the film is not extremely conductive then the lattice contribution must be left in Eq. 15, as it can be of the same order of magnitude as the conductivity. To elucidate this point we plot in Fig. 3 the transmission of a 500 nm free standing GaAs film. The solid lines show the exact transmission as calculated from Eq. 13 using the Drude–Lorentz model for σ (electron density $N = 1 \times 10^{18} \text{ cm}^{-3}$, scattering time $\tau = 100 \text{ fs}$) and Eq. 4 for $\epsilon_L(\omega)$ (same parameters as in Section 2.1). The dashed lines show that the transmission calculated using Eq. 16, i.e. ignoring the lattice contribution, is reasonable only in a narrow frequency range below 2 THz, whereas Eq. 14 (dash-dotted line) is in far better agreement with the exact transmission.

In order to assess the impact of neglecting the lattice contribution when the experimental transmission is used to determine the conductivity we calculated $\sigma' = (2/Z_0 d)[1/T - 1]$ using the exact transmission from Fig. 3. Shown in Fig. 4a and b are the real and imaginary parts of σ (solid lines) and of σ' (dashed lines). The function σ' clearly contains a contribution from the TO-phonon mode, and cannot therefore be modeled just by the Drude–Lorentz

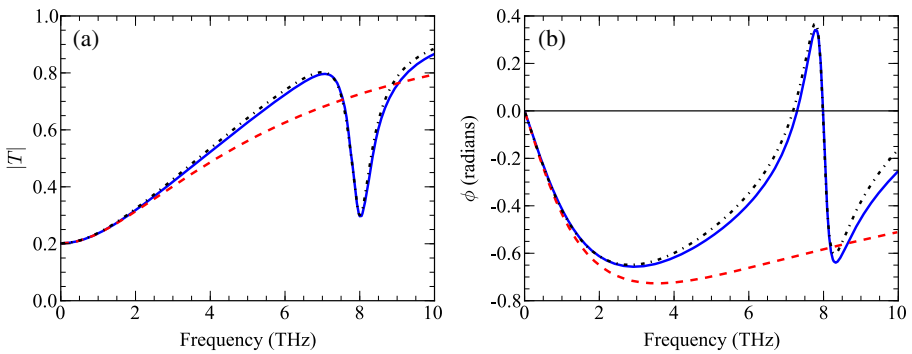


Fig. 3 **a** Absolute part and **b** phase of the transmission of a 500 nm thick GaAs film, calculated using Eq. 13 (solid lines) including the contribution from the TO phonon mode at 8.0 THz. The dash-dotted lines show the transmission in the thin-film limit from Eq. 14. The dashed lines indicate the transmission in the thin-film limit and neglecting the TO phonon (Eq. 16).

conductivity expression (Eq. 18). In particular, σ'_2 deviates from σ_2 significantly above 1 THz. In Fig. 4c and d this comparison is repeated for a less conductive GaAs film, with $\tau = 10$ fs. While the real part of σ' (dashed line in c) agrees with the actual conductivity (solid line in c) in the range up to 7 THz, the imaginary part of σ' (dashed line in d) is negative, rather than positive, and disagrees entirely with σ_2 (solid line in d). This pitfall becomes apparent for materials with low conductivity, and may be the source of some of the

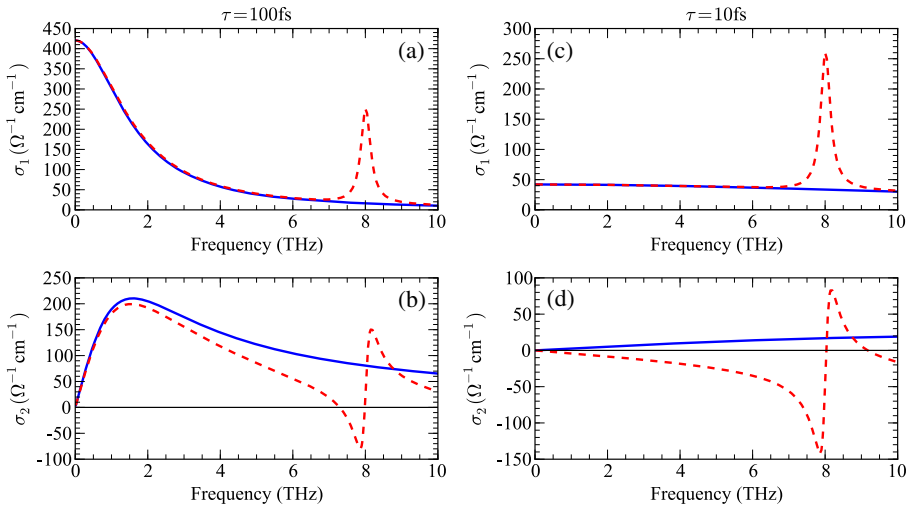
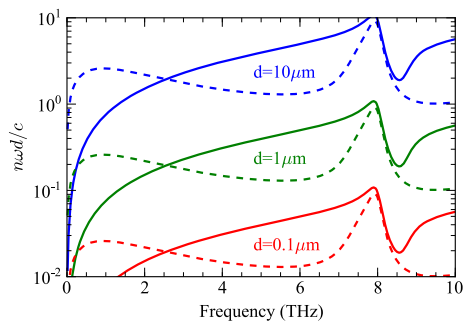


Fig. 4 **a** Real and **b** imaginary conductivity calculated from the transmission of n-type GaAs ($\tau = 100$ fs, as shown by the solid lines in Fig. 3). Here the conductivity calculated from Eq. 15 is shown by solid lines, and the dashed lines show $\sigma = (2/Z_0 d)[1/T - 1]$, i.e. neglecting the lattice contribution. **c** and **d** show the same as **a** and **b** but with a less conductive film where $\tau = 10$ fs.

Fig. 5 Plot of $n\omega d/c$ for various film thicknesses for undoped (solid lines) and n-doped GaAs (dashed lines, parameters in text). The thin film limit $n\omega d/c \ll 1$ is valid for GaAs when $d < 1 \mu\text{m}$.



negative imaginary conductivities often reported in the literature for inorganic semiconductor nanoparticles (Section 4.2) and polymers (Section 5.3).

We investigated the validity of the thin film limit by plotting in Fig. 3 the transmission of n-type GaAs (including the TO phonon, $\tau = 100 \text{ fs}$, $N = 10^{18} \text{ cm}^{-3}$) with the exact formula (Eq. 13, solid lines) and with the thin-film formula (Eq. 14, dash-dotted lines). The agreement is good over the whole frequency range for this thickness of GaAs (500 nm). To illustrate where the thin-film formula breaks down, i.e. where the limits $n\omega d/c$, $\kappa\omega d/c \ll 1$ are not valid, we plot in Fig. 5 the values of $n\omega d/c$ for undoped GaAs (solid lines, ϵ_L as above) and for n-doped GaAs (dashed lines, $\tau = 100 \text{ fs}$, $N = 10^{18} \text{ cm}^{-3}$) at three film thicknesses $d = 0.1, 1, 10 \mu\text{m}$. Below a thickness of $d = 1 \mu\text{m}$ the thin-film limit is satisfied, while for materials with higher dielectric constants or with resonances d may need to be even thinner.

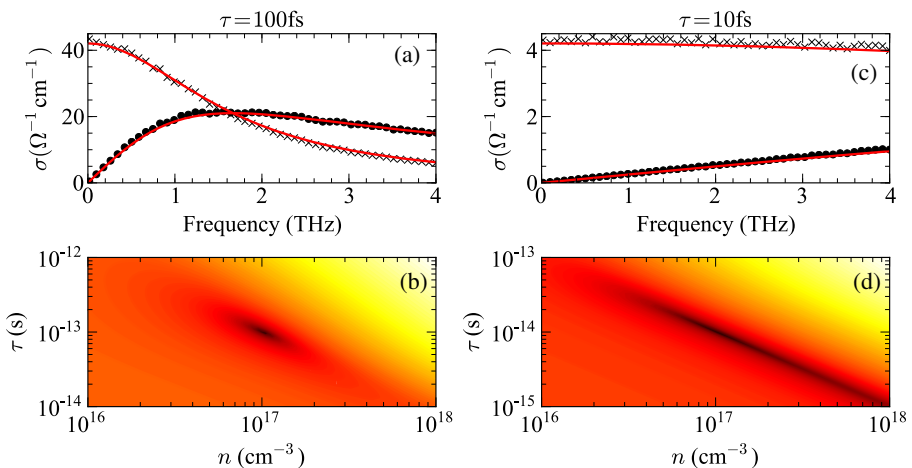


Fig. 6 **a, c** Real (crosses) and imaginary (points) parts of the conductivity of n-type GaAs ($N = 10^{17} \text{ cm}^{-3}$) using the Drude–Lorentz model (solid lines, Eq. 18) with **a** $\tau = 100 \text{ fs}$ and **c** $\tau = 10 \text{ fs}$, and 5% noise. **b** and **d** show the rms error between fit and $\sigma(\omega)$ in **a** and **c** using a range of N and τ (darker indicates a smaller rms error). When the plasma frequency is well above the frequency range, or τ is small, the conductivity can be modeled by a larger range of N and τ .

2.3 Accessible parameter range

Two-dimensional contour plots of the root-mean-square (rms) error between fit and experiment are convenient methods to visualise the significance of parameters extracted from a model. In Fig. 6a and c the complex conductivity for n-type GaAs with $N = 10^{17} \text{ cm}^{-3}$ is plotted, calculated from the Drude–Lorentz model (Eq. 18) with 5% random noise to simulate a typical experiment, with bandwidth 4 THz. In (a) the scattering time $\tau = 100 \text{ fs}$ produces a peak in σ_2 within the frequency range, and σ_1 decreases monotonically with frequency. When $\tau = 10 \text{ fs}$ σ_1 is substantially flatter (Fig. 6c), and the peak in σ_2 is well above the frequency range. In order to assess the ease of modelling this ‘experimental’ data, we plot in Fig. 6b and d the rms error between the ‘experimental’ data (in a and c) and the Drude–Lorentz conductivity calculated over a range of N and τ . A darker colour indicates a lower rms error and a better fit. While a sharp global minimum in the rms error can be seen in b for the $\tau = 100 \text{ fs}$ case, this minimum error is substantially extended along a range of N and τ when $\tau = 10 \text{ fs}$. This consideration illustrates that parameters (e.g. N , τ , or a resonance frequency) extracted from fits obtained using THz-TDS should be treated with care when no peak (or no rapid change) is observed in σ_1 or σ_2 over the measured frequency range.

3 Conductivity models

In this section we outline and compare various models of the THz conductivity, which are summarised in Fig. 7. We focus initially upon the THz conductivity of homogeneous media in order to elucidate the underlying physics of charge transport. In Section 3.1 we explore the Drude–Lorentz model and the limits of its applicability, before discussing phenomenological (Sections 3.2 and 3.3) and quantum mechanical (Sections 3.4 and 3.5) expressions for the conductivity at THz frequencies. A discussion of how to model the THz conductivity of inhomogeneous materials, such as blends of two or more constituents, is deferred until Section 3.6. Effective medium theories, quantum hopping models and Monte Carlo simulations are also mentioned in Section 3.6.

The form of the complex conductivity $\sigma = \sigma_1 + i\sigma_2$ can be examined by analogy with simple circuit theory. For a voltage wave of the form $V = V_0 e^{-i\omega t}$ the complex impedance of an inductor with self-inductance L is $Z_L = -i\omega L$, while for a capacitor it is $Z_C = i/(\omega C)$. A bulk semiconductor with a single charge carrier can be modelled as a non-polarisable material in which the current lags behind the applied electric field, i.e. a resistor R in series with an inductor L . The complex conductivity σ is proportional to the inverse of the complex impedance Z of this circuit, and therefore $\sigma \propto 1/Z = 1/(R - i\omega L) \propto R + i\omega L$. Both the real and imaginary parts of the complex conductivity of a bulk semiconductor would therefore be expected to be positive.

To examine the case of charge transport in a polarisable medium a capacitor C can be included in the equivalent circuit. For a capacitor and resistor in series

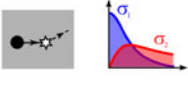
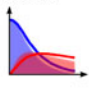
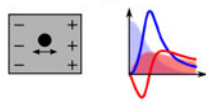
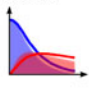
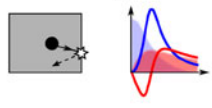
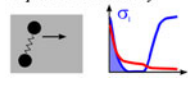
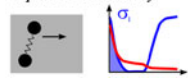
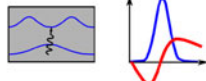
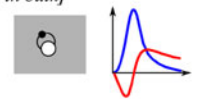
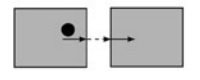
	Local conductivity models (homogeneous media)		Effective conductivity models (inhomogeneous media)
	Infinite media	Finite media	
Classical	Drude-Lorentz 3.1 <i>Mean scattering time τ</i>  Cole-Cole/Cole-Davidson 3.3 <i>Energy dependent τ</i> 	Plasmon 3.2 <i>Restoring force</i> <i>Polarisation field</i>  Smith 3.3 <i>Backscattering</i> 	Effective medium theory 3.6 <i>Composite media (e.g. metal in air)</i> <i>Simple sample shapes (e.g. spheres)</i>  Monte Carlo 3.6 <i>Non-equilibrium distributions</i> <i>Electrostatics & electrodynamics</i> <i>Quantum or classical particles</i> <i>Bandstructure, band bending etc.</i> <i>Arbitrary sample shapes</i> 
	Boltzmann 3.4 <i>Fermi-Dirac statistics</i> <i>Energy dependent τ</i> <i>Delocalised states</i> <i>Specific scatterers</i> Linear response theory 3.5 <i>Intraband</i> <i>Uses energy dispersion</i> Extended Drude 3.5 <i>Fermi liquids. Frequency dependent τ and m^*</i> Localisation modified 3.3 <i>Localised quantum states</i> Superconductors 3.5 <i>Gap in conductivity</i> 	Intersubband 3.5 <i>Quantum confinement</i> <i>Selection rules</i>  Excitonic 3.5 <i>Intra-excitonic transitions</i> <i>[larger binding energy in quantum wells, but also in bulk]</i> 	Hopping 3.6 <i>Quantum tunneling between grains</i> <i>Local conductivity model in grains</i> 

Fig. 7 Summary of various THz conductivity models. Local conductivity models can be subdivided depending on whether classical mechanics or quantum mechanics is applicable, and by whether they treat infinite or finite media. Approaches to treat inhomogeneous media are shown on the right. Key concepts are in *italic*, and the relevant sections in this article are referenced in *red*. Typical shapes for σ_1 and σ_2 are shown by blue and red lines, and the shaded areas make a comparison with the Drude-Lorentz lineshape.

the complex conductivity $\sigma \propto 1/Z = 1/(R + i/\omega C) \propto R - i/\omega C$ has positive σ_1 but negative σ_2 . A negative imaginary conductivity is therefore expected to be a characteristic of a polarisable medium, and can indeed be observed in a number of systems, as discussed in subsequent sections.

3.1 Drude-Lorentz model

The simplest model of the frequency-dependent conductivity of metals and semiconductors is provided by the Drude-Lorentz approach, in which an electron-hole plasma is treated as a non-interacting gas. Carriers undergo

collisions that randomize their momentum with a rate $\Gamma = 1/\tau$ that is assumed to be independent of energy. The Drude–Lorentz model assumes that the displacement x of a carrier (with effective mass m^* and charge q) from its equilibrium position is given by:

$$\frac{d^2x}{dt^2} + \Gamma \frac{dx}{dt} = \frac{qE_{\text{local}}}{m^*} \quad (17)$$

where at normal incidence the local electric field E_{local} of the THz pulse is related to the incident field E_{THz} by $E_{\text{local}} = 2E_{\text{THz}}/(n+1)$. Under a constant applied field carriers drift with velocity $qE_{\text{local}}\tau/m^*$. If the incident electric field oscillates at angular frequency ω , i.e. is of the form $E_{\text{THz}} = E_0 e^{-i\omega t}$, then the displacement can be assumed to have the same form $x = x_0 e^{-i\omega t}$. Substitution for x and E in Eq. 17 readily yields x_0 . The dielectric function ϵ can be determined from the definition of the polarisation $P = \chi \epsilon_0 E = Nqx$, and the conductivity is then (via Eq. 1)

$$\sigma(\omega) = \frac{Nq^2}{m^*} \frac{\tau}{1 - i\omega\tau}, \quad (18)$$

which has a peak in σ_1 at zero frequency and a maximum in σ_2 at $\omega = 1/\tau$. The conductivity for n-type GaAs ($m^* = 0.067m_e$, $\tau = 100$ fs, $N = 10^{17} \text{ cm}^{-3}$) is illustrated in Fig. 8.

While the Drude–Lorentz conductivity is adequate to model the intraband conductivity of some metals and semiconductors, it often fails as the electron scattering rate is in fact energy dependent, and bands are parabolic only close to extrema. A further constraint is that the material is uniform over the length scale that electrons explore during their motion. The limitations of this model can be readily exposed by the time-domain numerical solution to Eq. 17 for electrons in GaAs ($\tau = 100$ fs) subject to motion under a typical THz pulse, shown in Fig. 9a with peak amplitude 4 MVm^{-1} (40 kVcm^{-1}), comparable to that achieved in THz-TDS setups based on amplified Ti:sapphire lasers [11]. The solid line in panel b demonstrates that electrons accelerate in the opposite direction to the applied field and reach a maximum displacement of

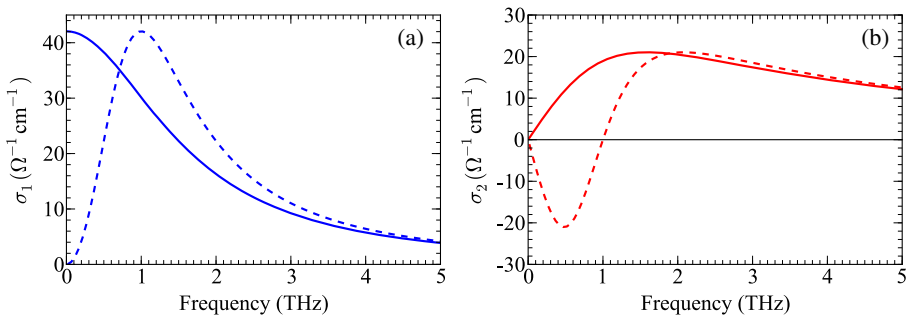


Fig. 8 **a** Real and **b** imaginary parts of the conductivity of n-type GaAs using the Drude–Lorentz model (solid lines) and the plasmon model (dashed lines).

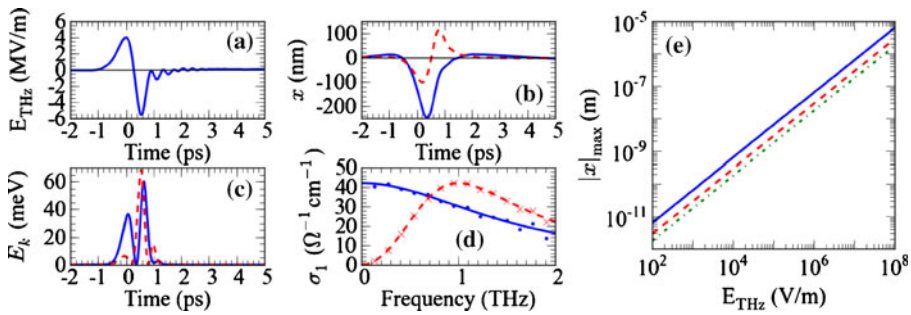


Fig. 9 **a** Incident THz electric field. The **b** displacement and **c** kinetic energy of electrons in GaAs are shown assuming the Drude–Lorentz model (*solid lines*) and the plasmon model ($f_0 = 1$ THz, *dashed lines*). **d** Real part of conductivity for the Drude–Lorentz (*solid line*) and plasmon (*dashed line*) models. **e** Maximum displacement $|x|_{\max}$ versus peak THz electric field for GaAs for the Drude–Lorentz (*solid*) and plasmon (*dashed*) models, and for the Drude–Lorentz model for ZnO and Si (*dash-dotted line*).

200 nm about 400 fs after the peak of E_{THz} . Electrons have a kinetic energy $E \sim 60$ meV during the negative half cycle of E_{THz} (panel c, solid line), greater than the LO-phonon energy $\hbar\omega_{\text{LO}}$. When an electron has an energy $E > \hbar\omega_{\text{LO}}$ it has a shorter momentum scattering time τ , as it can change direction by emitting an LO phonon. It is clear that for $E_{\text{THz}} > 4 \text{ MVm}^{-1}$ the THz pulse may accelerate electrons sufficiently to alter their scattering rate, and the Drude–Lorentz conductivity expression no longer suffices.

To validate the time-domain model we calculated the conductivity by using the Fourier transforms of $x(t)$ and $E_{\text{THz}}(t)$ in the expression $\sigma(\omega) = -iNq\omega x(\omega)/E_{\text{THz}}(\omega)$. The points in Fig. 9d show that σ_1 determined from this expression is in good accord with that derived for a monochromatic wave, Eq. 18 (solid line), as expected.

The magnitude of E_{THz} also places a stringent restriction upon the size of the material for which the Drude–Lorentz model may be expected to be valid. The maximum electron displacement $|x|_{\max}$ is shown in Fig. 9e as a function of E_{THz} . For pulsed THz spectroscopy based on low-field THz sources ($E_{\text{THz}} < 10^5 \text{ Vm}^{-1}$) the electron displacement remains below 2 nm. However at higher field strengths ($E_{\text{THz}} > 10^6 \text{ Vm}^{-1}$) $|x|_{\max}$ rapidly exceeds 100 nm, and consequently the Drude–Lorentz model will not be valid for a nanomaterial with a comparable extent in the direction parallel to the applied field. If the electron effective mass is higher, such as $m^* = 0.24m_e$ for ZnO or $m^* = 0.26m_e$ for silicon, the maximum displacement is lower (dash-dotted line, $m^* = 0.25m_e$). Having examined these limitations we now consider alternative THz conductivity models.

3.2 Plasmon model: Drude–Lorentz model with a restoring force

The plasmon model offers a straightforward extension to the Drude–Lorentz model. Here, the motion of electrons under a restoring force and an external

electromagnetic wave is described by the equation of motion of a damped, driven simple harmonic oscillator [27]. The restoring force can be provided electrostatically, for instance by a surface depletion or accumulation field, as is often found close to the interfaces of semiconductors. The plasmon model has therefore been applied to model the THz conductivity of semiconductor nanomaterials (Section 4.2). Equation 17 is altered by the addition of the term $\omega_0^2 x$ to the left-hand side, where ω_0 is the angular frequency of the oscillatory response. A larger restoring force requires a greater value of ω_0 . The conductivity in this model is

$$\sigma(\omega) = \frac{Ne^2}{m^*} \frac{\tau}{(1 - (i\tau(\omega - \omega_0^2/\omega)))}. \quad (19)$$

For particular geometries ω_0 can be linked to the plasma frequency $\omega_p = (Ne^2/m^*\epsilon_\infty\epsilon_0)^{1/2}$ by $\omega_0^2 = f\omega_p^2$. Under the assumption that charges are located on the surface of a small spherical particle the geometrical factor $f = 1/3$ [27], while for cylindrical wires $f = 0$ when the electric field \mathbf{E}_{THz} is axial and the wavevector \mathbf{q}_{THz} is radial, $f = 1/2$ when \mathbf{E}_{THz} and \mathbf{q}_{THz} are radial, and $f = 1/3$ for radial \mathbf{E}_{THz} and axial \mathbf{q}_{THz} [28, 29].

The influence of the restoring force upon electron motion in GaAs can be seen in Fig. 9b, where the plasmon rate equation was solved numerically with the same parameters as the Drude–Lorentz case, and with $\omega_0/2\pi = 1$ THz. The position x with a restoring force (dashed line) is a strongly damped harmonic oscillation about $x = 0$. The kinetic energy peaks slightly earlier than for the Drude–Lorentz model (panel c, dashed line). As the electron displacement is additionally restrained by the restoring force, the maximum x is lower than for the Drude–Lorentz model. This can be seen by the dashed line in Fig. 9e.

3.3 Phenomenological extensions to the Drude–Lorentz model

As established in Section 3.1, when an electron or hole's displacement under E_{THz} becomes comparable to the dimension L of the material (in the direction of E_{THz}) then the conductive response of the medium will differ significantly from that of the bulk material. A criterion for this to occur is that the electron or hole mean free path l should be greater than L , i.e. $l = v\tau > L$, where the carrier velocity is often equated with the thermal velocity $v = \sqrt{3k_B T/m^*}$. For room temperature electrons close to the Γ -valley minimum of GaAs $v \sim 5 \times 10^5 \text{ ms}^{-1}$ and $\tau \sim 100 \text{ fs}$, yielding $L < 50 \text{ nm}$. Similarly, for silicon ($m^* = 0.26m_e$, $v \sim 2 \times 10^5 \text{ ms}^{-1}$ and $\tau \sim 100 \text{ fs}$) the estimate is $L < 20 \text{ nm}$. In materials satisfying this dimensional constraint scattering from the interface may therefore be expected to play an important role. This argument, however, neglects three important considerations. Firstly, the carrier velocity v should not be equated to the thermal velocity, rather it is the Fermi velocity v_F – only electrons within $k_B T$ of the Fermi surface can scatter from an occupied to an unoccupied state. For materials photoexcited well above bandgap the mean carrier velocity will be a function of time, since the carriers will cool. Secondly, the THz electric field can give electrons significant kinetic energy when E_{THz}

is too high (see the time-domain model in Section 3.1 and Fig. 9). Finally, at $L < 50$ nm quantum confinement effects can also become significant: for instance in a GaAs quantum well with infinite barriers the spacing between the lowest two electron subbands is 1 THz when $L = 63$ nm. Phenomenological conductivity models that include the role of the interface will therefore be applicable when the average electron displacement approaches the sample's dimensions, but when quantum confinement is not yet significant (Fig. 10).

An extension to the Drude model aimed at modeling the conductivity of carriers undergoing restricted motion is that proposed by Smith [30], in which a carrier retains part of its initial velocity upon scattering. The collisions are assumed to be randomly distributed in time, and the fraction c_n of a carrier's initial velocity retained after p scattering events allows the Drude model to be generalized to

$$\sigma(\omega) = \sigma_D(\omega) \left[1 + \sum_{p=1}^{\infty} \frac{c_p}{(1 - i\omega\tau)^p} \right]. \quad (20)$$

Here, the term $\sigma_D(\omega)$ is the Drude conductivity of Eq. 18. For elastic collisions the parameter c_p is the expectation value $\langle \cos \theta \rangle$, for scattering angle θ . If the carrier's momentum is randomized then $c_p = 0$, while if it is completely backscattered then $c_p = -1$. Commonly, the infinite series in Eq. 20 is truncated at $p = 1$, which corresponds to the assumption that the carrier retains part of its initial momentum during the first scattering event, but in every subsequent scattering events the velocity is randomized. The phenomenological basis of this approach, however, limits the physical insight gained. In addition, with $c_1 = -1$ and $c_{p>1} = 0$ the Drude–Smith model can be seen to be identical to the surface plasmon model upon the substitutions $\omega_0^2 = 1/\tau_{DS}^2$, $1/\tau_{SP} = 2/\tau_{DS}$. The subscripts DS and SP distinguish the scattering times used in the Drude–Smith and surface plasmon models.

An alternative approach to understanding the conductivity of materials with length scales comparable to the mean free path is to include the effect of non-uniformity on the electronic states. In disordered materials electronic wavefunctions cannot be completely described by long-range delocalised

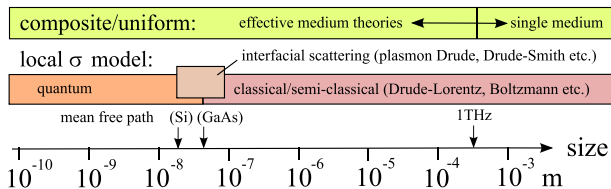


Fig. 10 Length scales of relevance for the THz conductivity of blends and micro/nanomaterials. When the material is non-uniform over length scales less than the diffraction-limited spot size ($\sim 300 \mu\text{m}$ at 1 THz) the optical properties of the composite should be considered, for instance using an effective medium theory. The choice for the local conductivity model of each constituent also depends on the length scale of the material, and the THz probe's electric field strength.

eigenstates such as Bloch functions. Disorder creates localised states that are better described by a tight-binding approach [31]. In the limit of weak disorder the first order correction to the Drude–Lorentz conductivity can be shown [31–34] to take the form

$$\sigma_1(\omega) = \text{Re}[\sigma_D(\omega)] (1 - A\tau^{-2} + (3\omega)^{1/2} A\tau^{-3/2}) \quad (21)$$

where the fit parameter $A = C/(k_F v_F)^2$ is given by the Fermi wavevector k_F , Fermi velocity v_F and a constant C of order unity [31, 34]. This conductivity expression is referred to as the localisation-modified Drude model, and can be derived from the quantum expression for the conductivity (Eq. 25) [31].

Other phenomenological extensions to the Drude–Lorentz model attempt to include the influence of an energy dependent τ . The Cole–Cole and Cole–Davidson models add exponents to the denominator of Eq. 18, producing

$$\sigma(\omega) = \frac{Ne^2}{m^*} \frac{\tau}{(1 - (i\omega\tau)^{1-\alpha})^\beta}, \quad (22)$$

where the Cole–Cole (α) and Cole–Davidson (β) parameters are in the range $0 < \alpha < 1$ and $0 < \beta < 1$. The Drude model is recovered in the limits $\alpha \rightarrow 0$, $\beta \rightarrow 1$. This expression can model small deviations from the Drude–Lorentz conductivity well, but does not provide insight into the dominant scattering mechanisms. Additionally, it cannot reproduce the negative imaginary conductivities reported in semiconductor nanomaterials (Section 4.2).

3.4 Boltzmann conductivity model

The conductivity models presented thus far (excluding Eq. 21) represent classical approaches where no account of quantum mechanical effects, such as a finite density of available states, or an energy dependent τ , has been made. Both of these contributions can be accounted for quantitatively by a generalised conductivity expression derived from the Boltzmann transport equation. In the relaxation time approximation under an external perturbation (such as an electric field) the rate of change of the electron distribution function is assumed to be inversely proportional to the scattering time τ . The Boltzmann transport equation in this approximation [35] can be used to derive the frequency dependent conductivity of an isotropic 3D material (with parabolic energy bands) as

$$\sigma(\omega) = \frac{2\sqrt{2m^*}e^2}{3\pi^2\hbar^3} \int_E \frac{\tau(E)E^{3/2}}{1 - i\tau(E)\omega} \left(-\frac{\partial f_0}{\partial E} \right) dE. \quad (23)$$

The electron distribution function in equilibrium at temperature T is given by the Fermi–Dirac distribution

$$f_0(E) = \frac{1}{e^{(E-\mu)/k_B T} + 1} \quad (24)$$

where the chemical potential μ can be determined numerically from the requirement that $N = \int_0^\infty f_0(E)g(E)dE$, where $g(E)$ is the electronic density

of states. The energy-dependent scattering time $\tau(E)$ can be calculated for various scattering mechanisms (e.g. with impurities, acoustic or optical phonons) by the application of Fermi's golden rule [36–38]. This approach has the benefit of turning the scattering time from a phenomenological fit parameter (as in the models above) into a quantity that can be determined from the carrier density. As the calculated $\tau(E)$ will depend upon the inclusion of the relevant scattering mechanisms this model gives insight into the underlying microscopic physics. In addition, conductivity can be seen to be a process only involving electrons with energies close to the chemical potential, as the function $\partial f_0/\partial E$ is peaked at μ [37]. This is in contrast to the classical models, where electrons with all energies contribute.

The Boltzmann conductivity expression has been applied in temperature-dependent THz-TDS studies of doped silicon [39] and doped GaAs [37] to examine deviations in the conductivity from the Drude–Lorentz form. It has also been applied to model the time-resolved photoconductivity of InAs [37].

3.5 Quantum conductivity models

Linear response theory (or Kubo–Greenwood theory) allows the conductivity associated with intraband and interband transitions to be determined. In essence, Fermi's golden rule is used to calculate the transition rate W_{ij} between an initial state i and a final state j , and $\hbar\omega W_{ij}$ is equated to the power lost by the electromagnetic field due to absorption [35, 36]. This yields the absorption coefficient α , from which the real part of the refractive index can be determined by the Kramers–Kronig relations. The resulting expression for the conductivity is

$$\sigma(\omega) = \frac{2e^2\hbar}{m^*2V} \sum_{ij} \frac{|\langle\psi_j|\hat{\mathbf{e}} \cdot \mathbf{p}|\psi_i\rangle|^2}{E_j - E_i} \frac{i[f(E_j) - f(E_i)]}{E_j - E_i - \hbar\omega - i\hbar/\tau} \quad (25)$$

where the unit vector $\hat{\mathbf{e}}$ points in the direction of the electric field \mathbf{E} , \mathbf{p} is the momentum operator and V is the volume over which the dipole matrix element $|\langle\psi_j|\hat{\mathbf{e}} \cdot \mathbf{p}|\psi_i\rangle|^2$ is taken. The matrix element creates selection rules for observable absorption peaks, for instance in semiconductor quantum wells intersubband absorption is only observed if the applied electric field is parallel to the direction of quantum confinement, and if the initial and final states have different parity. The quantum expression for the conductivity requires the wavefunctions ψ of the initial and final state to be known, and allows interband, intersubband, and intraband transitions to be treated within the same formalism. For intraband transitions in a parabolic band Eq. 25 reduces to the Boltzmann expression given in Eq. 23 [35]. For allowed intersubband transitions in quantum wells, such as absorption from the lowest state 0 to the next highest state 1 (separated by an energy E_{10}), the above expression can be simplified to yield the real part of the conductivity as [38, 40]

$$\sigma_1(\omega) = \frac{e^2 f_{10}}{2m^*} \int g(E) f(E) \frac{\hbar\Gamma(E)}{(\hbar\omega - E_{10})^2 + \Gamma^2(E)} dE, \quad (26)$$

where f_{10} is the oscillator strength and $\Gamma = \hbar/\tau$ is the linewidth in units of energy. In the limit of an energy-independent Γ this yields [40]

$$\sigma_1(\omega) \propto \frac{\Gamma}{(\hbar\omega - E_{10})^2 + \Gamma^2}, \quad (27)$$

which is plotted in Fig. 11a for $E_{10}/h = 2$ THz and $\tau = 300$ fs along with σ_2 obtained from the Kramers–Kronig relation.

Excitons are formed when electrons and holes bind together, and are most prominent in systems exhibiting quantum confinement, where the excitonic binding energy is enhanced. The eigenstates of an exciton can be modelled in comparison to the hydrogen atom, with states 1s, 2s, 2p, 3s *etc.* in spectroscopic notation. While the lowest order electric dipole allowed transition (1s–2p) falls in the UV range for hydrogen, the lower effective masses of electrons and holes in semiconductors and high dielectric constant results in a 1s–2p transition in the terahertz frequency range for excitons in e.g. GaAs quantum wells [41, 42]. Fermi's golden rule yields the frequency dependent complex conductivity as

$$\sigma(\omega) = \frac{N_X e^2}{m^*} \sum_k \frac{f_{j,k} \omega}{\omega_{j,k}^2 - \omega^2 - i\omega/\tau_X}, \quad (28)$$

where N_X and τ_X are the excitonic density and linewidth, the energy difference between the initial state j and final state k is $\hbar\omega_{j,k}$, and $f_{j,k}$ is the electric dipole matrix element for the transition [43, 44]. Figure 11b illustrates that the excitonic conductivity has a similar shape to that of an intersubband transition ($\omega_{1s,2p} = 2$ THz, $\tau_X = 170$ fs). The two mechanisms can be distinguished for example by the selection rule for intersubband absorption.

For superconductors the quantum mechanical expression for the conductivity is given by Mattis–Bardeen theory [45]. When the THz photon energy exceeds the Cooper pair binding energy 2Δ then strong absorption can occur, producing a σ_1 that increases with frequency above $\hbar\omega = 2\Delta$. The conductivity according to the Mattis–Bardeen theory is shown in Fig. 12 (solid lines) for $2\Delta = 10$ meV at $T = 10$ K. The two-fluid model [8, 46, 47] is often utilised to

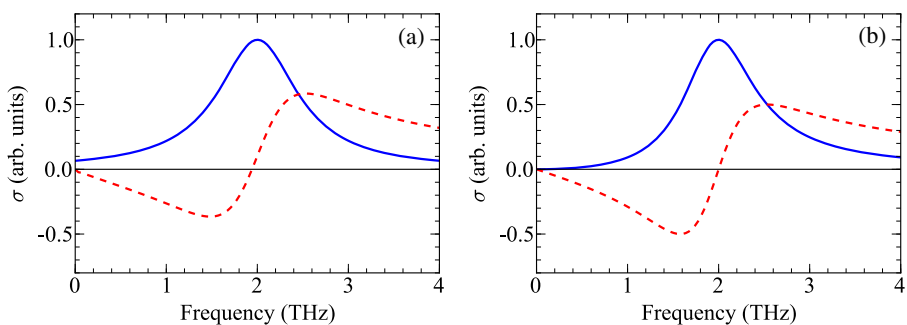


Fig. 11 Real (solid) and imaginary (dashed) parts of **a** the intersubband conductivity (Eq. 27) and **b** the intra-excitonic 1s–2p conductivity (Eq. 28), normalised to the peak of σ_1 .

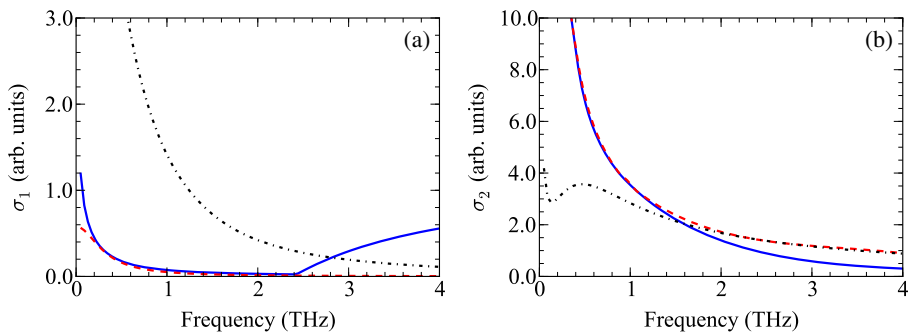


Fig. 12 **a** Real and **b** imaginary conductivity of a superconductor with energy gap $2\Delta = 10$ meV (2.4 THz) at 10 K according to Mattis–Bardeen theory (solid line). The dashed line indicates a fit using the two-fluid model ($x_s = 0.94$, $\tau = 510$ fs) to the sub-gap conductivity, showing that both σ_1 and σ_2 scale as $1/\omega$ at low temperature (low x_n). With a higher temperature ($x_n = 0.9$, $\tau = 300$ fs) the Drude–Lorentz peak in σ_2 at finite frequency emerges (dashed line) close to the superconducting transition temperature.

approximate the conductivity in the THz range, provided that the THz photon energy is well below the Cooper pair binding energy. The conductivity is the sum of a Drude–Lorentz term, arising from thermally excited carriers, and a superconducting term σ_s that is purely imaginary (as superconductors act as perfect inductors). At the superconducting transition temperature the fraction x_s of carriers in the superconducting state is zero, while at zero temperature the fraction x_n of thermally excited carriers is zero. The conductivity is given by

$$\sigma(\omega) = \frac{Ne^2}{m^*} \left[\frac{x_n \tau}{1 - i\omega\tau} + x_s \left(\frac{i}{\omega} + \pi\delta(\omega) \right) \right], \quad (29)$$

where N is the sum of the densities of the superconducting Cooper pairs and the normal carriers, and $x_n + x_s = 1$. The infinite dc conductivity in the superconducting state (produced by the delta function) creates a characteristic $\sigma_2 \propto 1/\omega$ dependence by the Kramers–Kronig relations. The dashed lines in Fig. 12 indicate that the two-fluid model provides a reasonable fit to the Mattis–Bardeen expression at 10 K. The dash-dotted lines show the emergence of the Drude–Lorentz conductivity shape at higher temperatures, using the two-fluid model with $x_n = 0.9$, $\tau = 300$ fs.

The extended Drude model [48, 49] provides an additional approach to describe the THz conductivity of quantum materials. It has been extensively applied to the visible and infrared conductivity of metals and superconductors, and is applicable for Fermi liquids with strong electron–electron interactions, rather than the weaker interactions of a Fermi gas. In this approach the single-particle effective mass m^* in Eq. 18 is replaced by a frequency-dependent function $m^{**}(\omega) = m^*[1 + \lambda(\omega)]$ and the energy-independent scattering time τ is replaced by a photon frequency dependent function $\tau^*(\omega)$. The effective

mass renormalization factor $1 + \lambda(\omega)$ can be determined from experiment using $m^{**}(\omega) = -Ne^2 \text{Im}[1/\sigma]/\omega$ if the electron density N is known [48, 49].

3.6 Effective conductivity of blends

The uniformity of the material in the directions perpendicular to the THz propagation wavevector is also of key importance. When the diffraction-limited spot size of terahertz radiation (1 THz = 300 μm in vacuum) is far larger than the material's dimension an effective medium theory (EMT), rather than a uniform medium, should be employed to model the composite material's dielectric function. Both micro- and nano-structured materials satisfy this restriction. When attempting to model a composite conductive material a suitable model for the optical properties of each constituent should therefore be chosen, and then combined using an effective medium theory, discussed at the beginning of this section. These considerations are summarised in Fig. 10. An additional concern is whether charge transfer can occur from one constituent to another: if so then the role of the interfaces (e.g. energy barriers, alignment of energy levels, gap thickness) may be important in determining the blend's effective conductivity. Hopping models and Monte Carlo simulations, which take into account charge transfer between different constituents, are discussed at the end of this section.

3.6.1 Effective medium theories

As an example of the importance of the use of effective medium theories in THz-TDS we consider the case of spherical particles of n-type GaAs embedded in a host medium with dielectric constant $\epsilon_h = 1$. For small volume fill fractions f Maxwell–Garnett theory is applicable, which enables the dielectric function $\epsilon^* = \epsilon_L^* + i\sigma^*/(\epsilon_0\omega)$ of the composite medium to be determined from

$$\frac{\epsilon^* - \epsilon_h}{\epsilon^* + 2\epsilon_h} = f \frac{\epsilon_p - \epsilon_h}{\epsilon_p + 2\epsilon_h}, \quad (30)$$

where the dielectric function of the particle is ϵ_p . The effective conductivity σ^* of the composite can be calculated from ϵ^* . Taking $\tau = 100$ fs and $f = 0.1$ yields the real and imaginary parts of σ^* as shown in Fig. 13 for $N = 1 \times 10^{17} \text{ cm}^{-3}$ (solid lines) and $N = 2 \times 10^{17} \text{ cm}^{-3}$ (dashed lines). A peak in σ_1^* , and a zero-crossing in σ_2^* , occurs as ϵ is changing rapidly with frequency in the range close to the plasma frequency (3.3 THz for the lower density and 4.7 THz for the higher density).

The shape of σ^* is comparable to that obtained from other conductivity models of uniform media, e.g. the plasmon, Drude–Smith and intersubband models. A simple consideration highlights the link between effective medium theories, which account for regions with different electric polarisation \mathbf{P} , and conductivity models such as the plasmon model. For a finite medium with uniform electric polarisation $\mathbf{P} = \chi\epsilon_0\mathbf{E} = (\epsilon - 1)\epsilon_0\mathbf{E}$ the bound volume charge

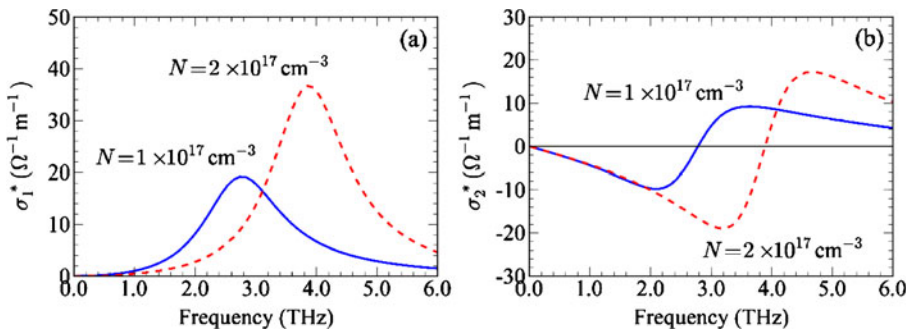


Fig. 13 **a** Real and **b** imaginary parts of the effective conductivity σ^* of an effective medium comprising spherical GaAs particles ($\tau = 100$ fs) in vacuum with fill fraction $f = 0.1$, with $N = 1 \times 10^{17} \text{ cm}^{-3}$ (solid lines) or $N = 2 \times 10^{17} \text{ cm}^{-3}$ (dashed lines).

density $\rho_b = \nabla \cdot \mathbf{P}$ is zero, but the surface charge density $\sigma_b = \mathbf{P} \cdot \hat{\mathbf{n}}$ is non-zero ($\hat{\mathbf{n}}$ is a unit vector normal to the interface). The electric field created by this surface charge density reduces the applied field by an amount that will be proportional to the surface charge density, and thus to the polarisation and to the displacement x . This is one origin of the $\omega_0^2 x$ term that has to be included in the equation of motion, as was done for the plasmon model in Section 3.2. The link between effective medium theories and the plasmon model is discussed further in [6] and [50].

One important extension to EMT was provided by Polder and van Santen [51], who generalised the theory to deal with ellipsoidal particle shapes, allowing cylinders and flat disks to be modeled. Maxwell–Garnet EMT is thought to not be accurate at high volume fill fractions f . In Bruggeman's alternative differential formulation of EMT [52] particle interactions were included, allowing blends with large f be explored. The effective conductivity ϵ^* of the blend is instead given by

$$f \frac{\epsilon_p - \epsilon^*}{g\epsilon_p + (1 - g)\epsilon^*} + (1 - f) \frac{\epsilon_h - \epsilon^*}{g\epsilon_h + (1 - g)\epsilon^*} = 0, \quad (31)$$

where the depolarising factor $g = 1/3$ for spherical particles. Scheller *et al.* recently reported an even more general effective medium theory that can model ellipsoidal particles with a distribution of sizes [53].

3.6.2 Hopping models

An alternative approach to model the THz conductivity of composite materials is to treat charge transport as consisting of an intra-particle and an inter-particle component. In arrays of closely spaced semiconductor nanocrystals there is a finite probability that electrons will tunnel quantum mechanically from one grain to another, thereby contributing to the conductivity. This model was developed by Dyre [54, 55] to account for the thermally activated conductivity of disordered solids, and has been applied to the optical conductivity of

metallic polymers [56] and recently to the THz conductivity of semiconductor nanoparticles [57]. The conductivity resulting from quantum tunneling can be written within the hopping model as

$$\sigma_h(\omega) = \frac{-\sigma_t i \omega \tau_t}{\ln(1 - i \omega \tau_t)} \quad (32)$$

where the expression for the dc tunneling conductivity $\sigma_t = N_t e^2 d^2 / (6 k_B T \tau_t)$ depends upon the spacing d between nanoparticles, the temperature T , the tunneling density N_t and the tunneling time τ_t . Note that this expression differs from that given in [55–57] because of the use of $e^{-i\omega t}$ herein, rather than $e^{i\omega t}$. The intra-particle conductivity $\sigma_p(\omega)$ was assumed to be described by the Drude–Lorentz model, and the effective conductivity of the composite σ^* was obtained by assuming the two channels combine in series according to

$$\frac{1}{\sigma^*(\omega)} = \frac{f}{\sigma_p} + \frac{1-f}{\sigma_h} \quad (33)$$

Here, f is the volume fill fraction of particles. As an example the hopping conductivity, Drude conductivity and effective conductivity are shown in Fig. 14 by the dotted, dash-dotted and solid lines, using $f = 0.84$, $\sigma_t = 5.7 \Omega^{-1} \text{cm}^{-1}$, $\tau_t = 0.4 \text{ ps}$, $\sigma_p(0) = 100 \Omega^{-1} \text{cm}^{-1}$ and $\tau = 20 \text{ fs}$. The real part of the hopping conductivity increases with frequency, as electrons gain more energy and become increasingly likely to tunnel through the barrier region between particles. In combination with the Drude–Lorentz model (peak in σ_1 at low frequency) this creates a resonant lineshape. These parameters for the hopping model differ from those in [57], and were chosen to produce agreement with a Drude–Smith (Eq. 20) fit to experimental data on photoexcited silicon nanocrystals [58], shown by the dashed line. The inter-particle/intra-particle approach therefore provides another alternative model that can create a resonance in the ac conductivity.

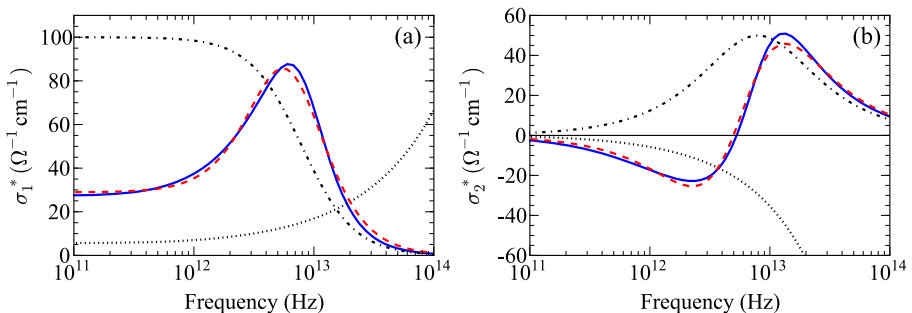


Fig. 14 **a** Real and **b** imaginary parts of the effective conductivity σ^* using the hopping model (solid lines, Eq. 33). The intra-particle and inter-particle contributions are shown by the dash-dotted and dotted lines. The Drude–Smith model with $c_1 = -0.83$, $\sigma_0 = 170 \Omega^{-1} \text{cm}^{-1}$ and $\tau = 26 \text{ fs}$ (dashed lines) was fitted to the experimental data (silicon nanoparticles, [58]). This figure follows Fig. 2 in [57], but used different fit parameters for σ^* .

3.6.3 Monte Carlo simulations of carrier dynamics

Monte Carlo simulations allow finite conductive materials to be modeled using discretised simulations involving particles, which move according to an equation of motion (e.g. Newtonian mechanics), and which have a probability of scattering in each time step. One benefit of a Monte Carlo simulation is that non-equilibrium situations can be modeled because each particle has a defined kinetic energy, and the energy-dependent scattering rates for energy and momentum relaxation can be included [36, 59]. Immediately after photoexcitation electrons have a non-equilibrium carrier distribution, with an electron energy distribution function that does not follow a simple expression (e.g. Maxwell–Boltzmann). In addition the Poisson equation can be solved at each time-step in order to account for changes in the static electric field within a material as charges move.

As an example of the application of full carrier dynamics simulations, we used the Monte Carlo model described in [16, 60] to simulate the electron distribution of GaAs at times after photoexcitation (50 fs pulse centred at 800 nm, photoelectron density of $N = 5 \times 10^{17} \text{ cm}^{-3}$, lattice temperature $T_L = 300 \text{ K}$). In Fig. 15a the simulated evolution of the electron distribution is shown at various times after photoexcitation (solid lines). The non-equilibrium Gaussian distribution of the laser pulse (see $t = 0$ curve) rapidly thermalises by carrier-carrier scattering within 200 fs to a Maxwell–Boltzmann distribution (dashed lines) that is equilibrated at a temperature above that of the crystal lattice. The solid and dashed lines in Fig. 15b show the electron and hole temperatures obtained from Maxwell–Boltzmann fits to the distribution. Electrons are cooled efficiently within 2 ps to close to the lattice temperature. The momentum scattering time (not shown) also changes dynamically, for instance

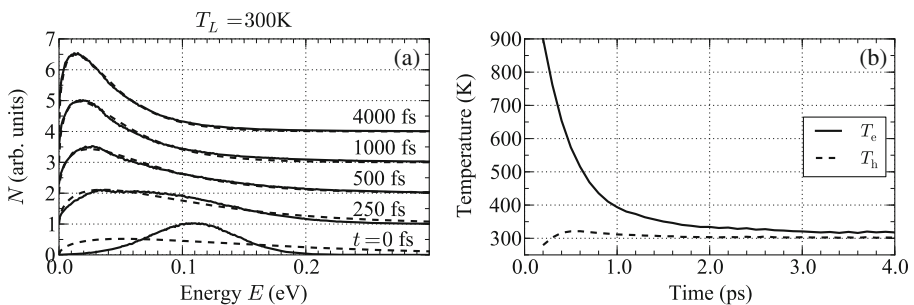


Fig. 15 Monte-Carlo simulation of the electron density in GaAs photoexcited at $N = 5 \times 10^{17} \text{ cm}^{-3}$, at a lattice temperature $T_L = 300 \text{ K}$. **a** Distribution of the kinetic energies of photoexcited electrons at various times after photoexcitation (solid lines, offset for clarity), and fits using the Maxwell–Boltzmann distribution (dashed lines). **b** Electron (solid line) and hole (dashed line) temperatures from fits using the Maxwell–Boltzmann expression to the simulated distribution.

because optical phonon emission is no longer possible once the distribution has cooled [60].

Monte Carlo methods have been used to understand various aspects of terahertz emission from photoexcited semiconductor surfaces [16, 60] and photoconductive antennae without [61–63] and including a solution to Maxwell's equations [64]. In recent years various simulations have modeled the THz conductivity of materials. The terahertz conductivity of doped silicon was examined using an ensemble Monte Carlo model coupled with a finite-difference solver of Maxwell's equations [65], and an excellent agreement with the non-Drude experimental conductivity was found. The dynamics of charge carriers in inhomogeneous semiconductors was studied using a simplified Monte-Carlo technique [66] that assumed carriers to have a thermal velocity, a constant scattering time, and to move in a constant potential [67]. Upon arriving at an interface charges were assumed to either pass unperturbed into the next nanocrystal, scatter isotropically (with an equal probability of entering either nanoparticle), or be reflected. The mobility ($\mu(\omega) = \sigma(\omega)/Ne$) was then calculated from the velocity distribution using the Kubo formula [68]. While a resonant conductivity was obtained in the THz range, analytical expressions for the conductivity of carriers confined in a potential well give similar lineshapes [69, 70].

Experimental studies of the THz conductivity of semiconductor nanomaterials are discussed in Section 4.2. One issue still to address is whether carriers should be treated classically or including quantum confinement. This will depend on the crystal quality of the nanomaterial: in an amorphous system quantum states are smeared out, and therefore treating carriers classically may suffice. In addition changes to the electrostatics of the charge distribution may contribute. The presence of surface depletion or accumulation fields created by surface states will influence carrier dynamics, and should be included by solving the Poisson equation self-consistently at each time step [16, 60]. This would be particularly beneficial in modeling OTP data, as the electrostatic potential within photoexcited regions will alter dynamically as the electron density changes with time.

4 Inorganic semiconductors

The terahertz frequency range is ideal for the investigation of doped semiconductors, as scattering times are typically in the range 50 fs–1 ps, and plasma frequencies also fall in the far-infrared. Many of the early, pioneering studies using terahertz time-domain spectroscopy were on bulk inorganic semiconductors. Immediately below we review the THz conductivity of doped inorganic semiconductors, before discussing micro- and nano-structured inorganic systems in Section 4.2. Studies of materials that exhibit quantum confinement are reviewed in Section 4.3.

4.1 Bulk

In the 1990s Grischkowsky and co-workers reported a comprehensive study of high resistivity [71] and doped [72] silicon using THz-TDS. They examined donor and acceptor levels in the range 10^{14} – 10^{16} cm $^{-3}$, both at room temperature and at 80 K [72]. For n-type Si a lifetime of 270 fs increased to 1.6 ps at 80 K. While the Drude–Lorentz model (Eq. 18) afforded a reasonable match with experiment, the Boltzmann conductivity integral (Eq. 23) achieved a closer fit. An energy dependent momentum scattering rate $\Gamma = 1/\tau$ was approximated using $\Gamma(E) = \Gamma_l(E/k_B T_0)^{1/2} + \Gamma_i(E/k_B T_0)^{-3/2}$. The parameters Γ_l and Γ_i are temperature and doping dependent scattering rates indicating the relative contribution of lattice and impurity scattering, respectively, and T_0 is a normalisation parameter with the dimension of temperature. In a subsequent study the Cole–Davidson model (Eq. 22 with $\alpha = 0$) was reported to provide a closer fit over a broader doping range (10^{13} – 10^{18} cm $^{-3}$) [39, 73], with $\beta = 0.8$ – 1.0 for n-type Si. A later study by Nashima *et al.* [74] over the temperature range 20 K–300 K reported a similar deviations from the Drude model, that became more pronounced at lower temperatures. Reflection geometry THz-TDS has also been utilised to study highly doped n-type Si at $N = 2 \times 10^{16}$ cm $^{-3}$ ($\tau \sim 190$ fs) [75] and $N = 3.5 \times 10^{16}$ cm $^{-3}$ [22]. Finally, Herrmann *et al.* [76] imaged Si wafers containing regions that had been ion-implanted to alter the doping type from n-type to p-type.

The THz conductivity of the direct-gap semiconductor GaAs was also first studied using THz-TDS by Grischkowsky's group in the 1990s [75, 77]. At room temperature and for n-type and p-type bulk GaAs $\sigma(\omega)$ was reported to agree well with the Drude model [77], with e.g. $\tau = 165$ fs at $N = 8 \times 10^{15}$ cm $^{-3}$. Subsequently, other groups extended the investigation to higher doping levels (10^{18} cm $^{-3}$) by examining thin films grown by molecular beam epitaxy [78].

An important step taken in the late 1980s and 1990s was to generate carriers optically with a fraction of the laser beam. This has the benefit of allowing the carrier density to be readily controllable, and also allows the photoconductivity to be measured on picosecond timescales after photoexcitation. Nuss *et al.* [79] investigated the photoconductivity dynamics of GaAs using a wafer attached to a LiTaO $_3$ film, which was also used to generate and detect the THz transient. The first free-space time-resolved optical-pump THz-probe experiment (using coherent generation and detection) examined the transmission change of GaAs photoexcited at 630 nm [80] by looking at the change in the peak of E_{THz} to produce a spectrally averaged response. The photoconductivity rise time was found to be <2 ps, and was demonstrated to be limited by the THz pulse duration. Subsequently InP [81] and InGaAs [82] were investigated using an interferometric technique rather than coherent detection. The spectral shape of the frequency dependent transmission change was modeled by the Drude–Lorentz formalism (e.g. for InGaAs $N \sim 3 \times 10^{15}$ cm $^{-3}$, $\tau \sim 110$ fs at 16 ps after photoexcitation [82]), and the photoconductivity rise time was found to lengthen when the photoexcitation wavelength decreased, providing electrons

with sufficient energy to reach the L and X side-valleys of the conduction band. The time-resolved transmission change of low-temperature grown GaAs was also reported [82], and the spectral dependence was found to agree satisfactorily with the Drude model ($\tau \sim 180$ fs) within 1 ps of photoexcitation [83]. Annealing the material at higher temperature was found to lengthen the photoconductive decay time, by reducing the density of electron traps [83].

In these early studies the photoinduced change in the THz transmission was either detected coherently but spectrally averaged [80], or obtained via interferometric techniques utilising a helium bolometer [81–83]. Flanders *et al.* reported the first study of the spectrally resolved photoconductivity of GaAs [84] that used coherent generation and detection, although the use of a cavity-dumped Ti:sapphire oscillator prohibited a large carrier density. Beard *et al.* [85] reported a comprehensive study of the photoconductivity of GaAs on picosecond timescales using an amplified Ti:sapphire ultrafast laser. The same group also studied low-temperature grown GaAs, with shorter photoconductivity decay times [86]. Importantly, the authors discussed how to ensure that each portion of the THz pulse experiences the same time delay with respect to the optical photoexcitation pulse. The authors used a finite-difference time-domain simulation to model the photoinduced transmission change ΔE_{THz} , by propagating the THz electric field pulse through the photoexcited medium [87], and highlighted the necessity of deconvoluting the detector's response before simulating ΔE_{THz} .

Since these groundbreaking studies the equilibrium and photoconductivity of bulk inorganic semiconductors remains a fertile, although well studied, area of research. The formation of quasiparticles from an electron-hole plasma was directly resolved in the time-domain for the first time in GaAs [88] and InP [89] using OPTP spectroscopy with mid-infrared probe pulses. Polarisation-sensitive THz-TDS in a magnetic field allows the carrier's effective mass to be determined for doped semiconductors, as the Lorentz force produces an off-diagonal component to the conductivity tensor [90, 91]. Other recent contributions have looked at the equilibrium conductivity of the wide bandgap semiconductors GaN [92] and ZnO [93–95], and the narrow gap alloy AlInN [96–98]. The influence of surface passivation on the time-resolved photoconductivity of GaAs has been investigated [99], with an enhancement in the photoconductive generation of THz radiation after chemical treatment. Another interesting development is the introduction of THz sources with sufficiently high electric field strength to accelerate electrons into side-valleys of the conduction band. Both optical-pump THz-probe and THz-pump THz-probe studies are reviewed in more detail in [6].

4.2 Micro- and nano-structured inorganic semiconductors

A number of investigations have been reported into the carrier dynamics of micro- and nano-structured inorganic semiconductors. In this section we focus upon studies of systems with dimensions larger than that expected to create quantum confinement.

One area of technological importance to which THz conductivity studies have contributed is in dye-sensitised nanoparticles for photovoltaic applications. Sintered networks of TiO_2 nanoparticles are often utilised as the electron transporting medium in dye-sensitised solar cells, which can exhibit quite high conversion efficiencies. Optical-pump terahertz-probe spectroscopy has been utilised by a number of groups to study the conductivity dynamics of dye-sensitised and bare TiO_2 nanoparticles [50, 67, 100–102]. Since typical TiO_2 particle diameters are between 20–30 nm, and the mean-free-path is of the order of 1 nm [50], the measured frequency-dependent optical functions of these blends are best described by a combination of the Drude–Lorentz model and an effective medium theory [50] (see Section 3.6). Electron transport in bulk rutile TiO_2 was found to be consistent with Feynmann’s polaron theory [103].

The equilibrium and photo-conductivity of semiconductors with sub-micron dimensions has been widely examined using THz-TDS. Silicon microcrystals (diameters $\phi = 1 - 30 \mu\text{m}$) were photoexcited at 800 nm, producing a uniform photoexcited carrier density in small particles and a density gradient in larger ones (the absorption depth is $\sim 10 \mu\text{m}$) [27]. The photoconductivity was modeled via the plasmon approach (Eq. 19). Given that the scattering time for electrons in silicon is of the order of $\tau \sim 190 \text{ fs}$ [22, 75] the mean free path estimated from the thermal velocity (Section 3.3) is $l \sim 40 \text{ nm}$, far smaller than the particle dimensions, and hence it cannot be argued that a local conductivity model based on interfacial scattering (e.g. the Drude–Smith approach) is applicable. The plasmon model can be justified based on electrostatic considerations, however, since the electrons close to one pole of the microspheres are constrained, and cannot be displaced under the THz electric field (Section 3.2). An alternative approach would be to use Maxwell–Garnett effective medium theory and the Drude model, which is conceptually similar (Section 3.6). The THz photoconductivity of isolated silicon nanocrystals with $\phi < 7 \text{ nm}$ [58, 104] has also been studied, much smaller than $l \sim 40 \text{ nm}$, and the Drude–Smith model was utilised to model the photoconductivity of the composite. Both σ_1 (positive) and σ_2 (negative) increased monotonically with frequency in the measured range.

In contrast, studies of the room-temperature photoconductivity of randomly oriented 50 nm-diameter GaAs nanowires [28] exhibited a resonant photoconductivity in the experimental range. This was attributed to a surface plasmon oscillation, rather than an intersubband transition or the Drude–Smith model, as the mode was observed to redshift with time after excitation, and to be fluence dependent. The presence of an AlGaAs shell, which helps to prevent the oxidation of the GaAs core, was shown to increase the photoconductivity decay time to $\sim 15 \text{ ps}$ [105], in comparison to $\sim 2 \text{ ps}$ without it.

A theoretical study of the THz conductivity of nanoparticles was carried out by Nemec *et al.* using a Monte Carlo model with a carrier mean-free-path $l = 10 \text{ nm}$ [66] (see also Section 3.6.3). For nanoparticles with dimensions of $3l = 30 \text{ nm}$ a resonance in the mobility spectrum was seen in the THz range, with a

shape similar to that produced by the Drude–Smith, plasmon and intersubband models. The same model was subsequently applied to TiO_2 [67], dye-sensitised TiO_2 and ZnO [106] and CdS [70] nanoparticles.

The THz equilibrium conductivity of honeycombs of porous silicon (pore diameters ϕ between 5 nm and 50 nm, film thicknesses d between 10 μm and 50 μm) [107] and porous InP ($\phi \sim 50$ nm, $d = 30$ μm) [108] were also studied. In the former study the thin-film limit was assumed in order to calculate ϵ analytically. In the latter study the conductivity of the membrane was calculated numerically from the transmission without assuming the thin-film limit, and a non-Drude conductivity was reported. However this was under the assumption that the dielectric constant was ϵ_∞ of the semiconductor [108], i.e. neglecting the reduction expected for an effective medium. Subsequently, the transmission was found to be well modeled by an effective medium model using the Drude–Lorentz expression for the semiconductor’s conductivity [109]. The photoconductivity of nanoporous InP was found to obey the Drude model [110]. Two-dimensional solutions to the Poisson equation were performed in order to examine the influence of conduction band bending close to surface states that pin the chemical potential [110]. Photoexcitation was found to dramatically increase the dark conductivity of nanoporous InP , perhaps as a result of a change in the surface pinning energy [109].

4.3 Quantum wells, wires and dots

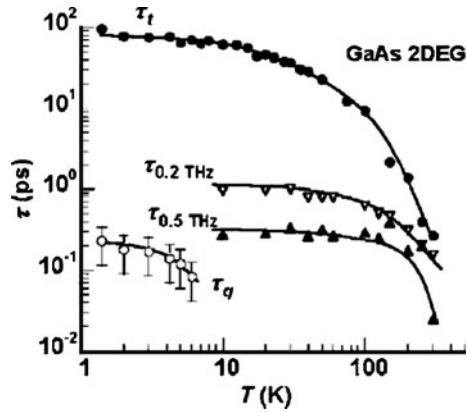
Inorganic semiconductor materials that exhibit quantum confinement in one (quantum wells), two (quantum wires) or three (quantum dots) dimensions have proven to be a fertile field of THz research in recent years. Here we discuss some research highlights for quantum wells, wires and dots.

The in-plane conductivity of GaAs and InAs two-dimensional electron gases (2DEGs) was reported by Kabir *et al.* [111]. The scattering time was obtained from the transmission T obtained using THz-TDS via the convenient relation

$$\tau = \frac{\sigma_2}{\omega\sigma_1} = \frac{1}{\omega} \frac{\text{Im}[1/T]}{\text{Re}[1/T] - 1}, \quad (34)$$

and was found to be weakly dependent upon the probe frequency, ranging from 1 ps at 0.2 THz to about 300 fs at 0.5 THz for GaAs [111], with similar lifetimes for InAs (Fig. 16). This can be understood to be a consequence of the non-Drude behaviour of the 2DEG system, because the left-hand equality of this expression is only valid if the conductivity takes the Drude–Lorentz form (Eq. 18). Surprisingly, this was substantially smaller than the scattering time of 90 ps obtained from dc transport measurements for GaAs . The discrepancy was explained by the suggestion that dc transport measurements preferentially select towards small-angle scattering events, in order for carriers to make it between contacts [111]. The THz scattering time was comparable to the quantum scattering time τ_q obtained from Shubnikov de Haas oscillations.

Fig. 16 The transport scattering time τ_t , THz scattering time at two frequencies, and quantum scattering time τ_q for a GaAs 2DEG as a function of temperature [111]. Reproduced with permission from Ref. [111]. Copyright © 2006, American Institute of Physics.



Lloyd-Hughes *et al.* [112] studied the in-plane mobility and electron density of the active regions and contact layers of quantum cascade structures. A precise knowledge of the conductivity of each layer is important in THz quantum cascade lasers (QCLs) in order to assess the waveguide losses of the material [113, 114]. Momentum scattering times were $\tau \sim 80$ fs and independent of temperature in the heavily doped contacts, while τ decreased from 1.6 ps at 4 K to 250 fs at 300 K for an active region with average doping $N = 2 \times 10^{16} \text{ cm}^{-3}$ [112].

The in-plane magnetoconductivity of 2DEGs and quantum well structures has been examined by a number of groups. In a pioneering study Huggard *et al.* [115] reported the THz transmission of a GaAs 2DEG under a magnetic field of 2.5 T normal to the layer. A semi-transparent gate contact allowed the application of a voltage to deplete the 2DEG, allowing the sheet carrier density to be modulated between $0 \leftrightarrow 8.8 \times 10^{11} \text{ cm}^{-2}$. The electron cyclotron resonance could be clearly seen in the time domain by looking at the differential THz electric field at the modulation frequency (Fig. 17a). The oscillatory response was fit in the time domain (solid line), yielding $\tau = 3.5 \pm 0.5$ ps. Additionally, by using a Michelson-interferometer to split and delay a portion of the THz generation beam, the authors demonstrated that they could send two independent THz pulses of equal magnitude onto their 2DEG sample [115]. This enabled the coherent control of the cyclotron oscillation, as can be witnessed by the differential transients in Fig. 17b, where the triangles illustrate the arrival times of the first and second THz pulse. In later studies, Wang *et al.* investigated the cyclotron resonance of GaAs 2DEGs and showed the conductivity in the frequency domain [116], and Lloyd-Hughes *et al.* reported the cyclotron resonance of photoinjected electrons in GaAs/AlGaAs quantum cascade structures [117]. Recently, a strong coupling between the cyclotron mode of a high mobility 2DEG and the photonic mode of a THz metamaterial has been demonstrated [118].

The out-of-plane electromagnetic response of semiconductor quantum wells, where intersubband transitions are dipole allowed, is of fundamental

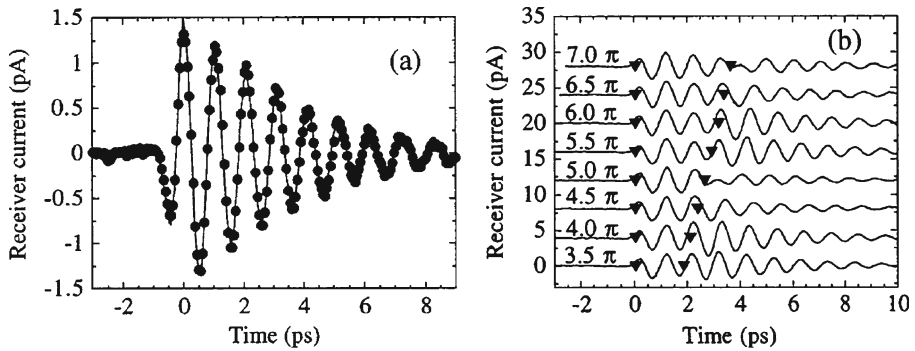


Fig. 17 **a** Differential THz electric field transmitted through a GaAs 2DEG at 5 K, under a 2.5 T magnetic field perpendicular to the 2DEG. The change in THz field results from the complete depletion of the 2DEG. **b** As in **a** but with two THz pulses arriving at times marked by the triangles. Traces are offset vertically for clarity [115]. Reproduced with permission from Ref. [115]. Copyright © 1997, American Institute of Physics.

importance for THz QCLs [114] and quantum well photodetectors. However, coupling free-space THz radiation to quantum well systems, with typical heights $\ll 10 \mu\text{m}$ is a significant challenge. In a seminal study, Kröll *et al.* demonstrated that THz-TDS can probe the intersubband absorption and gain of operating THz quantum cascade lasers [119]. The coupling to the sub-wavelength single-plasmon waveguide was achieved using a silicon lens attached to the facet of the QCL. The single-pass gain of the device was directly determined at the laser frequency, and was found to clamp above threshold [119]. Subsequent studies of quantum well heterostructures using THz-TDS [120–122] have demonstrated THz amplifiers with time-resolved switching of the gain [122], and have also investigated the coupling of THz pulses to metal-metal waveguides with strongly sub-wavelength heights [123]. Furthermore, the ultrafast interaction between electromagnetic radiation and a cavity-coupled mode in the strong coupling regime has been examined using mid-infrared time-domain spectroscopy of quantum wells in a waveguide [124].

The interaction of THz radiation with excitons, in which an exciton can be promoted e.g. from a hydrogenic 1s to a 2p state (Section 3.5), has been investigated by a number of groups. Groeneveld and Grischkowsky reported a time-resolved transmission change at 2.0 THz indicative of an excitonic response, after the resonant photoexcitation of 10 nm GaAs quantum wells with $\text{Al}_{0.33}\text{Ga}_{0.67}\text{As}$ barriers [41]. With a photoexcitation energy in the conduction band the excitonic resonance was observed to rise over the course of 100 ps, due to the formation of excitons from unbound electron-hole pairs. Kaindl *et al.* reported the photoconductivity of excitons in slightly larger GaAs quantum wells (14 nm), with a consequently lower exciton binding energy and 1s–2p transition frequency of 1.7 THz [42]. They presented their photoinduced changes using $\Delta\sigma_1$ and $\Delta\epsilon_1$, and studied the excitonic decay under resonant

excitation, and non-resonant formation under continuum excitation. Subsequent studies examined the onset of a Drude–Lorentz conductivity contribution that becomes apparent at higher pump fluences [43, 44], when the excitons either dissociate or act intrinsically like a free electron-hole plasma due to the overlap of adjacent wavefunctions. The application of a magnetic field was found to split the degeneracy of the excitonic 2p state, producing two resonances in $\Delta\sigma_1$ that diverged with increasing magnetic field [117].

The THz photoconductivity of free-standing quantum dots (also called nanoparticles) has been examined in depth. Time-resolved photoconductivity measurements were used to investigate the degree of coupling between disordered arrays of InP nanoparticles with a 3.2 nm mean diameter. The photoconductivity was observed to increase by a factor of six when the interparticle distance decreased from 1.9 nm to 0.8 nm [125]. Beard *et al.* [126] reported that the photoconductivity of nanoparticles of CdSe with diameters from 2.5–25 nm could be well described by the combination of the Drude–Lorentz model and Bruggeman effective medium theory. An alternative description was given by Wang *et al.* who attributed the photoinduced change in the THz transmission of colloidal CdSe quantum dots (1–10 nm diameter) to a strongly bound exciton [127]. An investigation of the Auger mechanism of electron-hole energy transfer in CdSe quantum dots was also reported [128]. Epitaxially-grown quantum dots embedded in a semiconductor matrix have also been studied by THz-TDS [129–133], as have quantum wires and posts [134, 135].

5 Organic materials

Carbon can be made into very long chains of interconnecting carbon-carbon bonds which are strong and stable. Four interesting allotropes of carbon in THz research are graphene, graphite, carbon nanotubes, and buckminsterfullerenes (buckyballs). Graphene is a plane of carbon atoms in 2-dimensions, as shown in Fig. 18 [136]. When graphene is stacked in three dimensions the material is called graphite. When the graphene is wrapped into cylindrical form or wrapped into a sphere (i.e. a soccer ball of hexagons and pentagons), the allotropes are termed carbon nanotubes and buckyballs respectively.

5.1 Graphene

Recently, the optical and electronic properties of graphene have come under intense scrutiny. Graphene is thought to exhibit a gapless, linear energy band dispersion close to the Dirac point. Graphene based devices such as (field-effect) transistors [137], terahertz generators [138, 139], and electronic and optical sensors [140, 141] are also research topics of extreme interest. In order to build devices, the characteristics of carriers in graphene should be fully understood. THz time-domain spectroscopy (THz-TDS) is an ideal tool to characterise the conductivity of graphene as it is a non-contact and non-

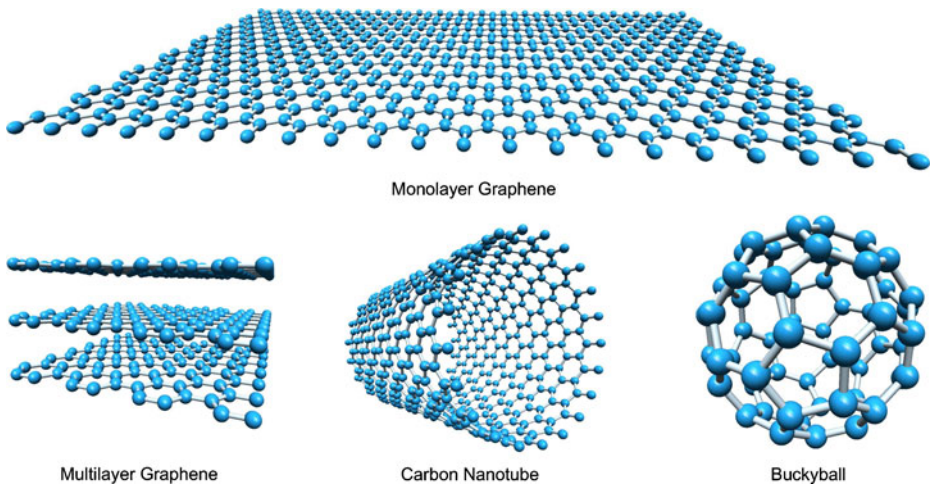


Fig. 18 The structure of monolayer and multilayer graphene, carbon nanotubes and buckyballs.

destructive method. In stark contrast to conventional semiconductor materials, THz radiation can promote interband transitions as well as intraband transitions in graphene [142], due to its negligible bandgap.

The broadband infrared and THz response of graphene has been studied by transmission spectroscopy [143–146] and ellipsometry [147]. In [146] the graphene layers were grown on a Si-terminated face of semi-insulating 6H-SiC wafers. The relative transmission spectra of nominally buffer, single-layer, and multi-layer graphene films (as measured by Fourier-transform infrared (FTIR) spectroscopy and THz-TDS) are shown in Fig. 19. The relative transmission was determined from the transmitted electromagnetic power ratio between samples with graphene on substrate ($T(\omega)$) and without graphene on substrate

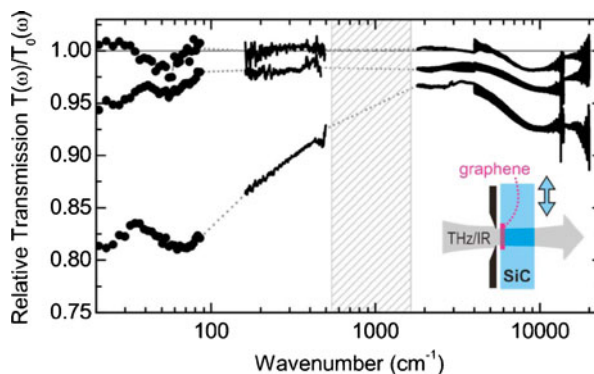
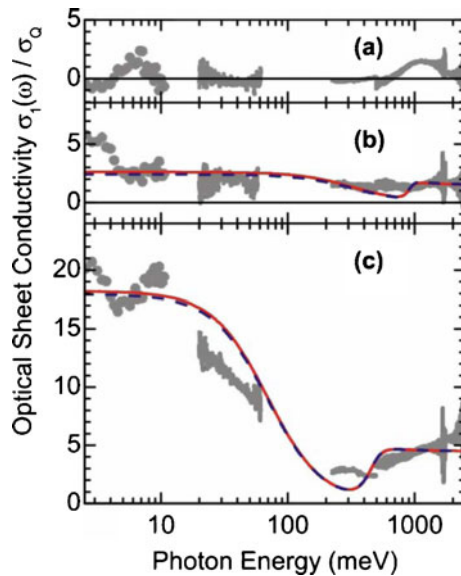


Fig. 19 Relative transmission of nominally buffer, monolayer, and multilayer graphene (*top to bottom*), measured by FTIR (*solid lines*) and time-domain THz spectroscopy (*dots*). *Dotted lines*: guides to the eye. *Hatched area*: Reststrahlen region of SiC. *Inset*: sample modulation scheme [146]. Reproduced with permission from Ref. [146]. Copyright © 2009, American Institute of Physics.

Fig. 20 Real part of the optical sheet conductivity (gray) of graphene, normalized by $\sigma_Q = \pi e^2/2h$ for **a** buffer layer, and **b, c** ‘monolayer’ and multilayer graphene with the buffer conductivity subtracted. Solid and dashed lines indicate theoretical calculations [146]. Reproduced with permission from Ref. [146]. Copyright © 2009, American Institute of Physics.



($T_0(\omega)$). The multi-layer graphene has a smaller transmission than single-layer graphene. Figure 20 shows the optical sheet conductivity of the three samples. The conductivity of multi-layer graphene is strongly frequency dependent. The calculated absorption of single- and multi-layer graphene was above 4000 cm^{-1} in the near-IR region and that of multi-layer graphene was below 500 cm^{-1} in the far-infrared.

Because of the very high absorption coefficient of single-layer graphene, the THz imaging and spectroscopy of large-area monolayer graphene is possible. Figure 21 illustrates recent THz images of a $15 \times 15\text{ mm}^2$ single-layer graphene film on a silicon wafer [148]. The graphene is clearly resolved against the background of the Si substrate. Figure 21b and c show an image of an edge and the relative transmission for a cross-section of the edge. The authors measured the relative transmission spectra for the first and the second THz pulses internally reflected within the substrate. By fitting the measured relative transmission, they determined the sheet conductivity of their graphene layer to be $\sigma_s = 2.04 \times 10^{-3}\Omega^{-1}$ in the THz frequency range.

Like semiconductor materials, the carrier concentration and distribution in energy are important parameters affecting the time-resolved conductivity of graphene [143, 146]. George *et al.* [143] measured the electron-hole recombination times in graphene using optical-pump terahertz-probe spectroscopy. Their epitaxially grown graphene samples consisted of approximately 12 carbon atom layers on 6H-SiC. The optical properties of epitaxial graphene are more similar to those of monolayer graphene rather than that of graphite [144], indicating that interlayer coupling between the carbon sheets may be negligible. When exposed to a 14.8 nJ, 800 nm optical pulse the measured real part of the complex amplitude transmission is as shown in Fig. 22a. When the optical pump pulse illuminates the graphene, the transmission decreases

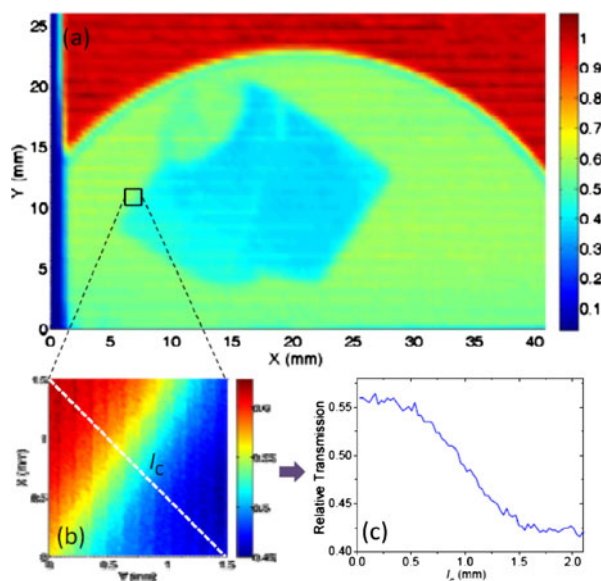


Fig. 21 **a** THz transmission image of the graphene-on-Si sample over a $26 \times 41 \text{ mm}^2$ region (pixel size is 0.4 mm). The graphene film and the Si substrate are shown in *light blue* and *bright green*, respectively. The *red* and *dark blue* regions correspond to air and the aluminum sample mount, respectively. Measurements were made at room temperature in ambient conditions. **b** A higher definition image ($1.5 \times 1.5 \text{ mm}^2$) taken with 0.02 mm steps shows an edge of the graphene. **c** The transmission along a cross-section of the edge (*white line* in **b**) is shown [148]. Reproduced with permission from Ref. [148]. Copyright © 2011, Optical Society of America.

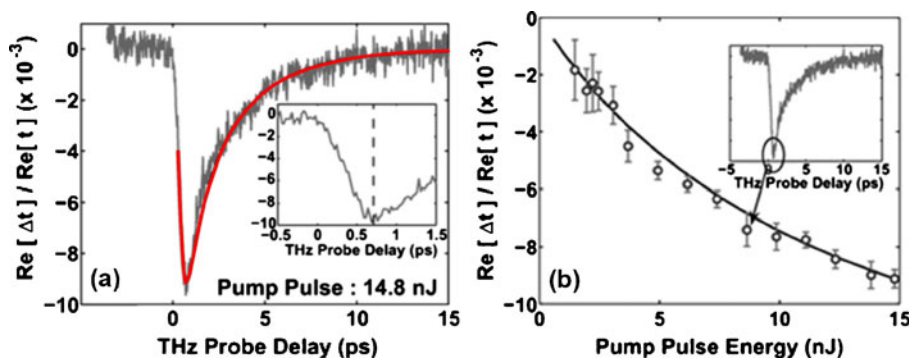
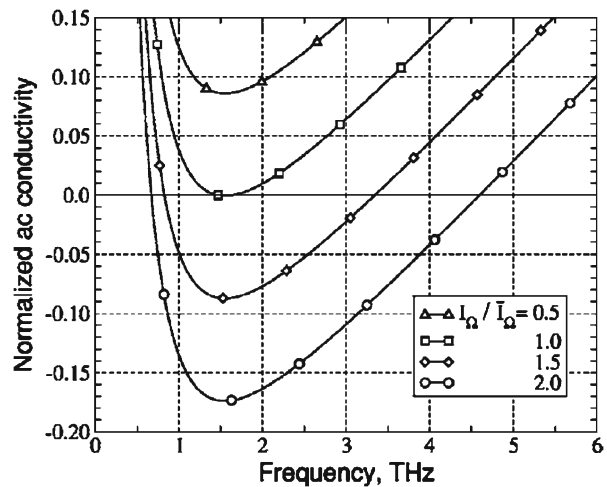


Fig. 22 **a** The measured change in the real part of the complex amplitude transmission (*black*) and the theoretical fit (*red*) for a pump pulse energy of 14.8 nJ . The transmission decreases rapidly until $0.75\text{--}1 \text{ ps}$ and then increases slowly from $1\text{--}15 \text{ ps}$. The *inset* shows the initial rise in the transmission, which occurs on a time scale longer than the experimental resolution of 130 fs . **b** The measured and predicted peak change in the real part of the complex terahertz transmission for different pulse energies [143]. Reproduced with permission from Ref. [143]. Copyright © 2009, American Chemical Society.

Fig. 23 Frequency dependence of normalized ac conductivity at different intensities of optical radiation [138]. Reproduced with permission from Ref. [138]. Copyright © 2007, American Institute of Physics.



dramatically before gradually increasing due to electron-hole recombination. As the optical pump pulse energy is varied from 1 nJ to 15 nJ, increasing the carrier concentration, the resulting peak change in the THz transmission increases sub-linearly (Fig. 22b). The transmission change after photoexcitation was calculated from a carrier dynamics model consisting of a set of coupled rate equations. The calculated values (solid lines in Fig. 22) when interband recombination and carrier cooling were included in the model produced a good fit to the experiment. In contrast, Choi *et al.* [146] reported a linear fluence-dependent transmission change for monolayer and multilayer graphene, over the range 0.1–0.9 μJcm^{-2} , and similar recombination times (1 ps). By calculating the relative magnitude of the photoinduced conductivity change arising from electrons and holes they report that their transmission change is dominated by the holes [146].

Recently, the non-linear optical response of graphene in the THz region has been studied by theoretical calculations [138, 142, 149] and experiment [142]. In particular, Ryzhii *et al.* [138] show theoretically that graphene can have a negative ac conductivity in the THz frequency range. When a sufficiently strong optical pump pulse is supplied, interband and intraband transitions can create a population inversion and negative ac conductivity (gain), as shown in Fig. 23 [138]. If the intensity of optical radiation (I_Ω) increases beyond its threshold value (\bar{I}_Ω) the ac conductivity (calculated at 77 K with an electron and hole momentum relaxation time $\tau = 1$ ps) has negative values over a broad frequency range. This effect might be used in graphene-based coherent sources and amplifiers of THz radiation, and recent experimental evidence has been reported in [142].

5.2 Carbon nanotubes

Carbon nanotubes are classified as either single-walled nanotubes (SWNTs) or multi-walled nanotubes (MWNTs), and have a cylindrical nanostructure.

When a graphene sheet is rolled to form a carbon nanotube (CNT) the electronic properties are determined by the pair of indices (n, m) , which are the number of unit vectors along two directions of the graphene lattice. If $n = m$ it is termed an armchair nanotube, and has metallic properties. Otherwise $m = 0$ (zigzag) nanotubes and $n \neq m$ (chiral) nanotubes have semiconductor properties [150]. The dielectric properties of SWNTs have been studied by electromagnetic waves up to 0.5 THz [151]. Carbon nanotube based THz devices such as THz detectors [152–154] and THz polarizers [155, 156] have been reported.

Although each SWNT has metallic or semiconducting characteristics the characteristics of films containing nanotubes with a variety of (n, m) cannot be explained by a simple Drude model. To analyse the conductivity of SWNT films, a combination of a Drude model and a Lorentzian oscillator was introduced as [157, 158]

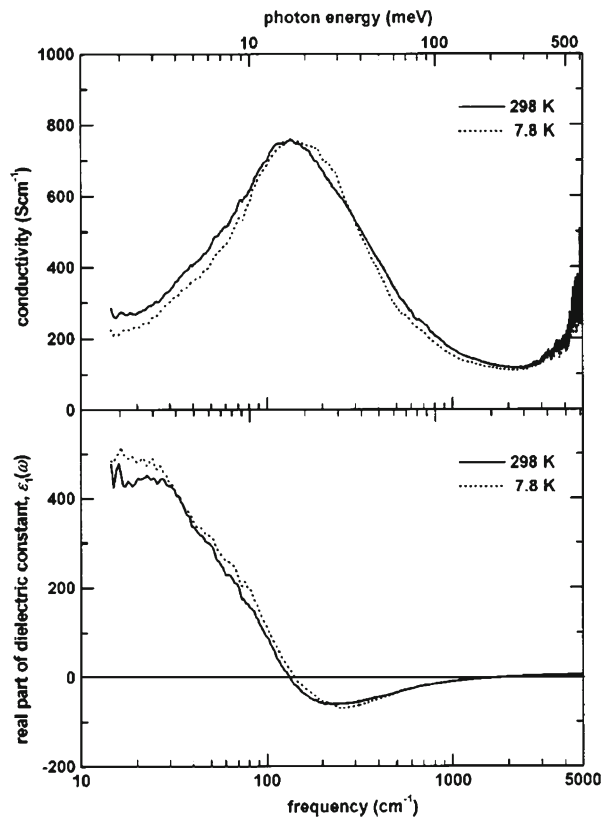
$$\epsilon_p(\omega) = \epsilon_{\text{Drude}} - \sum_j \frac{\omega_{p,j}^2}{\omega^2 - \omega_j^2 + i\Gamma_j\omega}, \quad (35)$$

where ϵ_{Drude} is the Drude contribution, and the sum over each Lorentzian oscillator j requires the parameters of the resonance frequency ω_j , plasma frequency $\omega_{p,j}$ and relaxation rate Γ_j . The values of σ_1 and ϵ_1 obtained by a Kramers–Kronig transformation of the reflectance measured by FT-IR over the range 15–5000 cm^{-1} is shown in Fig. 24 [157]. Just a single Lorentzian at $\omega_j/2\pi = 4$ THz was required to adequately model the THz conductivity. The real part of the dielectric function is negative from 145 cm^{-1} to 1680 cm^{-1} because of the localized conductivity band at 135 cm^{-1} . The measurements of DC conductivity are 220 $\Omega^{-1}\text{cm}^{-1}$ at 298 K and 160 $\Omega^{-1}\text{cm}^{-1}$ at 7.8 K which agrees well with that estimated from the above expression to within 5%.

Most carbon nanotube films are comprised of bundles of randomly distributed CNTs that form networks. The conductivity of the film therefore contains an intratube and an intertube contribution. Moreover the CNTs are embedded in a dielectric medium such as air, and an effective medium theory is more appropriate. Indeed, the real conductivity of CNT films increases with increasing frequency [155]. Both the Maxwell–Garnett model (Section 3.6, Eq. 30) [155, 158–161] and the Bruggeman model (Section 3.6, Eq. 31) [162] were utilized to interpret the results. The dielectric function of the effective medium was calculated taking the dielectric function of the nanotube (particle) constituent from Eq. 35, and air as the host medium. Slepian *et al.* [163] highlighted the influences of an axial depolarization field (due to the finite nanotube length) and surface curvature upon the effective THz conductivity of SWNT composites. A weak temperature dependence of the THz conductivity was explained by the variation of the chemical potential within an ensemble of different SWNTs [164].

Additional studies of the THz and mid-infrared conductivity of SWNTs have been performed using pump-probe spectroscopy [164–168]. When the SWNTs are excited by a laser pulse whose optical energy is bigger than 10 meV,

Fig. 24 Real parts of the conductivity [σ_1] (*top*) and dielectric function [ϵ_1] (*bottom*) of a SWNT film, obtained by a Kramers–Kronig analysis of the reflectance [157]. Reproduced with permission from Ref. [157]. Copyright © 1999, American Physical Society.



interband transitions produce a change in the THz conductivity that can be attributed to an exciton-induced reduction in the mobility of free carriers [166].

MWNTs consist of multiple rolled layers (concentric tubes) of graphite, with consequently different mechanical and electrical properties compared with SWNTs. Often SWNTs have higher aspect ratios (defined as the ratio of length to diameter) than MWNTs, resulting in a higher conductivity for SWNTs compared with that of MWNTs [162]. MWNTs contained in a deformable rubber were also studied at varying density (up to 5.0% by weight), with an increasing absorption and dispersion at higher loading levels [169].

Recently, the optical and electrical properties of various CNTs including SWNTs, double-walled carbon nanotubes (DWNTs), MWNTs, and graphene oxide (GO) with and without various nanocrystals was investigated by THz-TDS [170]. The real conductivity of the hybrid nanostructures was found to decrease in the order SWNT > DWNT > MWNT \approx GO. The reduction in conductivity was attributed to an increased trapping of electrons at surface defects formed during nanocrystal growth.

Meanwhile, anisotropic (aligned) SWNT films have been studied with polarised THz beams [155, 158] because individual SWNTs make excellent conductors with very long coherence lengths and extremely uniform diameter

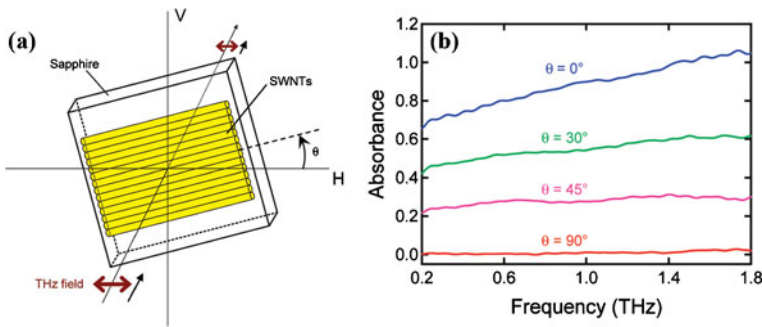


Fig. 25 **a** The experimental scheme for the characterisation of a polarizer made from an aligned SWNT film on a substrate and **b** THz absorbance for different polarization angles (coloured lines) [156]. Reproduced with permission from Ref. [156]. Copyright © 2009, American Chemical Society.

[156], and strong absorption. Aligned films were obtained by mechanically squeezing a SWNT slurry on an undoped silicon window using a bar coater. The polarization-dependent THz transmission measurements were performed for the aligned SWNT film. The Maxwell–Garnett model was used to analyse the characteristics of the aligned SWNT film, with good agreement in the THz frequency range. When the aligned SWNT film and the THz beam polarization are parallel, the absorption and dispersion are bigger than when they are perpendicular. Although the extinction ratio was not extremely high, this research showed the possibility of using SWNTs in THz polarizers.

Recently THz polarizers were demonstrated using a highly aligned, 2 μm thick SWNT film on a sapphire plate [156] and a 9 μm thick free-standing MWNT sheet [171]. Figure 25a illustrates the experimental scheme for the polarization state measurements and b shows the absorbance for the measurements, which increases close to $\theta = 0$ and is a weak function of frequency. The characteristics are good, but do not provide a high extinction ratio with

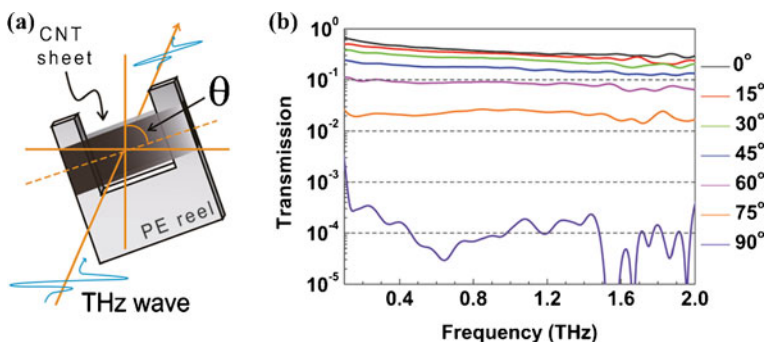


Fig. 26 **a** The experimental scheme for the characterisation of a polarizer consisting of a free-standing MWNT sheet and **b** THz transmission spectra for various polarizer angles (coloured lines) [171]. Reproduced with permission from Ref. [171]. Copyright © 2011, American Chemical Society.

this film thickness. However, Kim *et al.* [171] reported a free-standing MWNT polarizer as shown in Fig. 26. Their experimental scheme for the polarization state measurements is shown in Fig. 26a, while panel b shows the transmission spectra for various polarizer angles. The average transmission at zero degrees is over 50% while a 4 order of magnitude suppression was observed at $\theta = 90^\circ$. Interestingly, a recent optical-pump THz-probe spectroscopy study by Xu *et al.* [167] examined SWNTs selectively excited using a polarized pump pulse, and suggested that unaligned SWNT films can act as transient THz polarizers.

5.3 Polymers

Conducting and semiconducting polymers are scientifically and industrially interesting organic materials because they can exhibit optical and electronic properties that can be readily controlled. It is challenging, however, to measure the electrical characteristics by traditional electrical measurements such as four-point probe measurements or Hall-effect measurements due to contact effects at metal/polymer interfaces. Non-contact spectroscopic studies using THz-TDS are invaluable in determining both the absorption and dispersion of the samples. The refractive index and absorption coefficient have been measured via using THz-TDS for conducting polypyrrole [172], poly-3-methylthiophene (P3HT) [32, 173, 174] and other polythiophenes [174] with different doping levels. Although the conductivity of polymers depends on doping level as for inorganic semiconductors, conduction in polymers occurs along one-dimensional delocalised bands formed by hybridised covalent bonds. Polymer chains are locally distorted by the presence of a charge carrier, and hence it is energetically favourable for carriers to localise [175], forming spin 1/2 polarons (charge and lattice distortion) or spinless bipolarons (polaron pairs) [175] rather than single electrons or holes.

The ac conductivity $\sigma(\omega)$ for the heavily doped conducting polymer polypyrrole was reported to obey the Drude model [172] with $N = 2 \times 10^{21} \text{ cm}^{-3}$ and $\tau \sim 0.6 \text{ fs}$. At lower doping levels the ac conductivity of conducting polymers does not, however, follow the simple Drude–Lorentz model [34]. For example, the THz conductivity of doped P3HT was found to exhibit a non-Drude shape [32, 173], and was analysed in terms of the localisation-modified Drude model (Eq. 21, Section 3.3). The theoretical fit was determined by three parameters: the plasma frequency $\omega_p/2\pi = 525 \text{ THz}$, scattering rate $\Gamma/2\pi = 520 \text{ THz}$ (collision time of $\tau = 8 \text{ fs}$), and $C/(k_f v_f)^2 = 0.36 \times 10^{-28} \text{ s}^2$.

At an increasing doping level, the characteristics of the polymer change from insulating to more metallic. Unuma *et al.* measured the THz pulses transmitted through free-standing films of p-doped regioregular P3HT, regiorandom P3HT and poly(3,4-ethylenedioxythiophene) (PEDOT) [174]. The amplitude of the THz transmission decreased with increasing doping levels, due to a higher conductivity. The complex conductivity spectra of the samples are shown in Fig. 27a, which were fit with the Drude–Smith model (see Eq. 20 and [30]) with $-1.0 < c_1 < -0.7$ and $c_{n>1} = 0$. The filled and open circles show real and imaginary parts of conductivity, respectively, calculated

from Eq. 6 and Eq. 7 under the assumption that the lattice contribution to the dielectric function is given by the mid-infrared dielectric constant of the undoped polymer, i.e. $\epsilon_L(\omega) = \epsilon_\infty \sim 2.45$ [174]. However, the presence of infrared-active vibrational modes and π -band to polaron band transitions creates absorption in the THz and mid-IR ranges [174] that necessitates (e.g. via the Kramers–Kronig relations) a larger $\text{Re}[\epsilon_L]$ in the THz than that in the midinfrared. The reported negative σ_2 may therefore just arise from a choice of ϵ_L that is too low (Eq. 7). Additionally, the use of $\sigma_2 = \omega\epsilon_0(\epsilon_\infty - n^2 + \kappa^2)$ in [174] implies that the conductivity function includes the phonon/lattice contribution (Section 2.1). However in that case a conductivity model based on just free carriers, such as the Drude–Smith model, cannot be justified. While the measurements and theoretical calculations are in good agreement in the THz frequency range, equally good agreement may perhaps be obtained with a number of conductivity models, e.g. the quantum hopping model (Eq. 33). Figure 27b shows that the relaxation time does not change substantially with carrier density for P3HT and PEDOT conducting polymers at different doping densities. This indicates that the slope of the optical properties in the THz range is roughly constant with doping. The carrier relaxation times are constant at around 12 fs, similar to that of P3HT measured by Jeon *et al.* [32, 173].

The interaction between charge carriers and visible light in semiconducting polymers is important for their use in optoelectronic devices. Optical-pump terahertz-probe spectroscopy has been used in a number of studies to examine the photoconductivity of semiconducting polymers. Hendry *et al.* [176] assessed the quantum efficiency η of charge carrier generation following photoexcitation of MEH-PPV, finding that the primary product was Frenkel excitons (tightly bound), with a small fraction of free charges ($\eta < 10^{-2}$) decaying within a few picoseconds. The authors used the Clausius-Mossotti equation to link the photoconductivity to the excitonic polarisability. Subsequently, the same group compared the photophysics of MEH-PPV in dilute solution with

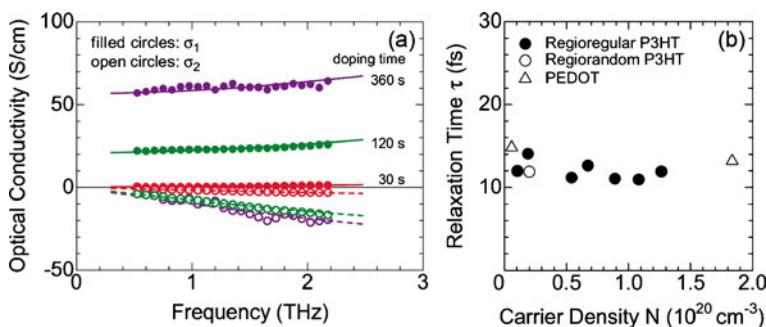


Fig. 27 **a** Complex conductivity spectra $\sigma(\omega)$ of regioregular P3HT (circles) prepared with doping times of 30 s, 120 s, and 360 s. Also shown by the solid lines are Drude–Smith conductivity fits to $\sigma(\omega)$. **b** Dependence of momentum relaxation time τ on carrier density N for regioregular P3HT (filled circles), regiorandom P3HT (open circle), and PEDOT (open triangles) [174]. Reproduced with permission from Ref. [174]. Copyright © 2010, American Institute of Physics.

that in the solid-state, finding that free charge generation was lower in solution ($\eta < 10^{-5}$) as a result of the reduced interchain coupling [177]. In regioregular P3HT charge carriers were found to be substantially longer lived, existing for nanoseconds [178].

Prins *et al.* [179] measured the intrachain mobility of charge carriers in poly(p-phenylenes) using time-resolved microwave spectroscopy. They showed that the conductivity depends strongly on the length of the polymer chain and that interchain interactions can severely decrease the intrachain mobility. A one-dimensional diffusive model (with carrier motion restricted by infinite potential barriers) was developed to obtain the mean-square particle displacement, and thus the mobility via the Kubo formula [68].

One early challenge facing the development of field-effect transistors based on semiconducting polymers was that charge trapping during normal device operation increased the threshold voltage for transistor action [180]. By measuring the transmission of polymer transistors fabricated on doped silicon Lloyd-Hughes *et al.* examined the charge trapping rate [181], and subsequently investigated the dissociation of excitons in the accumulation layer under continuous wave excitation [182].

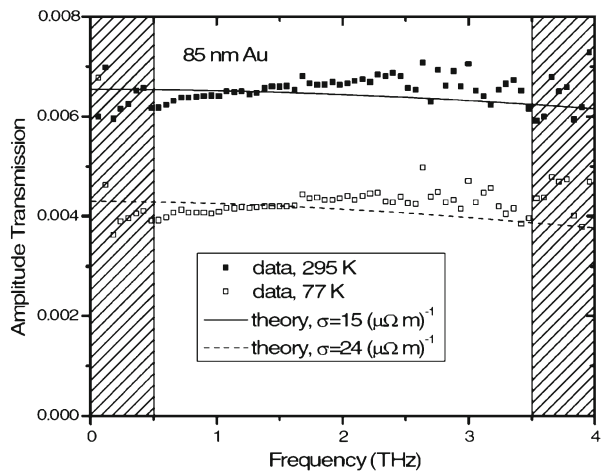
For photovoltaic applications of semiconducting polymers it is important to maximise the generation of charge carriers. Polymer-fullerene blends have been studied in great depth, and can produce device efficiencies of several percent. Ai *et al.* determined the charge generation efficiency of bulk heterojunctions created from blends of P3HT with the functionalised fullerene PCBM [183]. While the initial ($t < 2$ ps) generation of charges was not altered by the addition of PCBM, the charge carrier decay was slower with the fullerene than just for the polymer. The efficient generation of a photoconductive response in P3HT-PCBM blends using strongly subgap photoexcitation (1.55 eV) has also been studied [184, 185]. In blends of the lower bandgap copolymer APFO-3 with PCBM, Nemec *et al.* reported that unbound charge carriers and bipolarons provide the major contribution to the THz transient photoresponse [186]. In a recent study Cooke *et al.* investigated charge carrier generation in roll-to-roll processed P3HT:PCBM solar cell structures that also contained ZnO and PEDOT:PS layers [187]. Using broadband THz pulses centred at 4 THz, the photoconductivity generation time was found to be less than 100 fs, and the fraction of mobile charges generated was estimated to be 20%.

In single-crystal organics such as pentacene carrier dynamics has also been investigated by THz-TDS [188–192], with an increasing photoconductivity at low temperature suggestive of transport in delocalised bands rather than thermally-activated hopping.

6 Metallic thin films

The conductivity of ultrathin metallic films is an important parameter for applications of THz surface plasmons and metamaterials. Recently, the thickness and temperature dependent THz conductivity of metal films was measured

Fig. 28 Amplitude transmission through 86 nm Au film at 295 and 77 K [193]. Reproduced with permission from Ref. [193]. Copyright © 2008, American Institute of Physics.



[193, 194]. Because thin metal films cannot stand freely in air the films were deposited on a high-resistivity silicon substrate, and THz transmission measurements were performed by THz-TDS. Unlike bulk metals, thin metal films have additional electron scattering mechanisms, from defects, grain boundaries, and surfaces [193]. Therefore the conductivity of a thin metal film is lower than that of a bulk metal [195].

Figure 28 shows the amplitude of transmission of an 85 nm-thick Au film at different temperatures [193]. The measured conductivity at room temperature is $15 \times 10^4 \mu\Omega^{-1} \text{ cm}^{-1}$. For thinner Au films ($< 15 \text{ nm}$) the metal does not coat the substrate uniformly, preferring to form islands, as investigated by Walther *et al.* [194]. The thinner Au films have lower conductivity, as shown in Fig. 29. To analyze these non-uniform media, the authors applied Bruggeman effective medium theory (EMT) where the only fit parameter was the fraction p of metal. The depolarisation factor in Eq. 31 was taken to be $g = 0.68$ as the metallic particles were elongated rather than spherical ($g = 1/3$). A Drude–Lorentz fit to the measured conductivity of a thicker gold film determined the plasma frequency $\omega_p/2\pi = 2080 \text{ THz}$ and the scattering time $\tau = 18 \text{ fs}$, and these parameters were assumed for the dielectric function of the metal regions. The agreement between experiment and theory was good for films with long-range conduction pathways (thickness $d > 8 \text{ nm}$), as illustrated by the conductivity in Fig. 29. The extracted values of p agreed with that from scanning electron microscopy. The EMT approach also worked satisfactorily for $d < 6 \text{ nm}$. However, for intermediate thicknesses $6 < d < 8 \text{ nm}$, corresponding to the percolative transition between long-range dc insulating and conducting behaviour, the EMT model could not fit σ_1 and σ_2 simultaneously. The authors instead adopted the Drude–Smith model, which was found to give a better fit to the data in this range. Interestingly, the lifetime τ was found to be enhanced close to the percolative transition, reaching 80 fs [194]. However, the EMT may also have fit the data if τ was allowed to vary. Similar films have been used as broadband THz anti-reflection coatings [196].

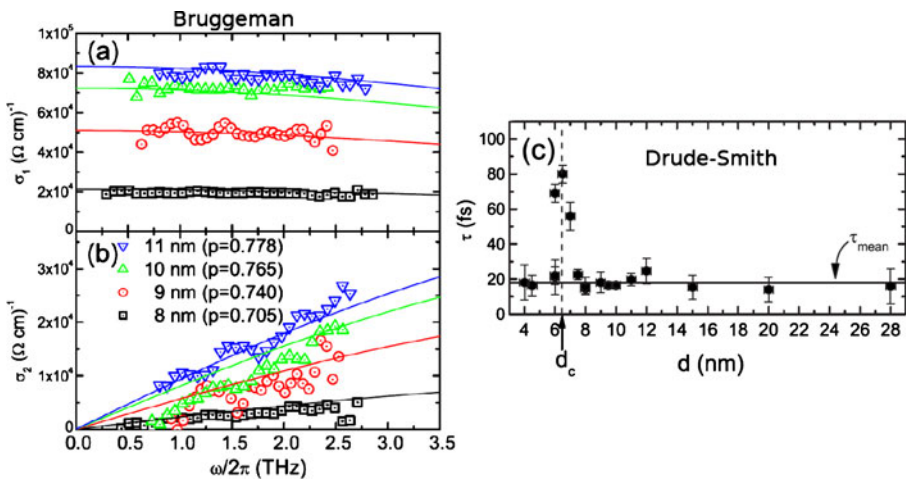


Fig. 29 **a** and **b** Terahertz conductivity spectra showing σ_1 and σ_2 for gold films of various thicknesses d above the percolation threshold $d_c = 6.5$ nm (points). The solid lines are fits according to Bruggeman EMT, yielding best-fit parameters for p as indicated. **c** Alternative Drude–Smith fits to the experimental data yield a lifetime τ that peaks at the percolative transition [194]. Reproduced with permission from Ref. [194]. Copyright © 2007, American Physical Society.

7 Strongly correlated systems

Substances with electrons that cannot be described as non-interacting particles are broadly termed “strongly correlated” systems. They often exhibit unique properties, such as magneto-electric coupling, colossal magnetoresistance and superconductivity, and offer novel functionality and applications. As with less exotic compounds, the interaction of THz radiation with strongly correlated systems provides a wealth of information. As the bulk of the THz conductivity studies have been performed on superconductors we discuss those first, and subsequently in Section 7.2 we review work on other strongly correlated materials.

7.1 Superconductors

In superconductors the electron-phonon interaction produces loosely bound pairs of electrons called Cooper pairs. While the dc conductivity of a superconductor becomes infinite when it is cooled below the superconducting transition temperature T_c , the optical properties (in the midinfrared and visible) of the superconductor do not change substantially [26]. This suggests that the low frequency electrical response tracks the superconducting order, while the high frequency properties are less informative. The THz frequency band is of interest because typical Cooper pair binding energies are $2\Delta \sim 1 - 10$ meV. As described in Section 3.5, at zero temperature and for $0 < \hbar\omega \leq 2\Delta$ superconductors exhibit a purely imaginary conductivity, while for photon energies above 2Δ photons can be absorbed (σ_1 is finite).

Advances in the understanding of the far-infrared/THz conductivity of superconductors have arrived sporadically. Early FTIR spectroscopy studies of σ of elemental superconductors such as lead and tin were performed in the 1950s and 1960s [26, 197, 198], and were instrumental in helping to validate the BCS theory of superconductivity. The development of THz-TDS, which coincided with the flurry of interest in high- T_c cuprate superconductors, led to a number of studies during the 1990s. THz-TDS has the benefits of allowing the direct examination of σ_1 and σ_2 , removing Fabry–Perot reflections, and also of allowing the recovery of the superconducting condensate after perturbation using an intense infrared pulse to be studied.

Nuss *et al.* used THz-TDS to study the superconducting band gap of bulk niobium [199], and reported a superconducting bandgap of 380 GHz (1.6 meV), with good agreement between their data and Mattis–Bardeen theory. Thin films of the cuprate $\text{YBa}_2\text{Cu}_3\text{O}_{7-\delta}$ ($T_c = 88$ K) were investigated by Spielman *et al.* [200], who used polarised THz transmission measurements in a magnetic field to measure a Faraday geometry rotation to the THz pulse, which they explained using the Hall effect. Subsequently, the same authors demonstrated that a model of the dynamics of vortices including an anisotropic energy gap was essential to model their frequency-dependent conductivity [201]. For films of $\text{Ba}_{0.6}\text{K}_{0.4}\text{BiO}_3$ the characteristic $\sigma_2 \propto 1/\omega$ was also observed [202], and although the measured frequency range was well below the superconducting gap 2Δ was obtained by fitting the imaginary conductivity using $\sigma_2/\sigma_n = (\pi \Delta/\omega) \tanh(\Delta/2k_B T)$, where σ_n is the normal state conductivity immediately above T_c [203]. Additional studies of the YBCO system [47, 204] used the two-fluid model (Eq. 29) to understand the conductivity. The conductivity gap in MgB_2 films ($T_c = 34$ K) was found to be $2\Delta = 5$ meV [205], roughly half the value expected for an isotropic BCS superconducting gap, which provided evidence for an anisotropic order parameter.

Recently the discovery of superconductivity in the iron containing pnictides has stimulated further investigations of σ using THz-TDS [206, 207]. Valdés Aguilar *et al.* demonstrated that contrary to the expectation from Mattis–Bardeen theory [45] the real conductivity of $\text{BaFe}_{1.84}\text{Co}_{0.16}\text{As}_2$ thin films does not tend to zero at low temperatures in the frequency range down to 0.2 THz. The real and imaginary parts of σ are shown in Fig. 30 at frequencies from 220 GHz to 440 GHz, and temperatures from 2 K to 25 K. While Mattis–Bardeen theory (solid lines) works satisfactorily at low frequency and temperatures close to $T_c = 21$ K, the disagreement with the experimental σ_1 and σ_2 (points) is pronounced, and may indicate an order parameter with an extended s-wave symmetry [206]. A similar conclusion was reached simultaneously by Fischer *et al.* [207] for $\text{Ba}(\text{Fe}_{0.9}\text{Co}_{0.1})_2\text{As}_2$, who deduced that a two-gap model with $2\Delta = 6$ meV and $2\Delta = 16$ meV was consistent with their THz conductivity spectra.

The photoinduced destruction of the superconducting condensate is a topic of fundamental physical interest that was first addressed experimentally in 1992 by Federici *et al.* [208]. A thin film of lead was photoexcited at 2.0 eV using an excitation fluence of $\sim 1 \mu\text{Jcm}^{-2}$. The spectrally resolved transmission

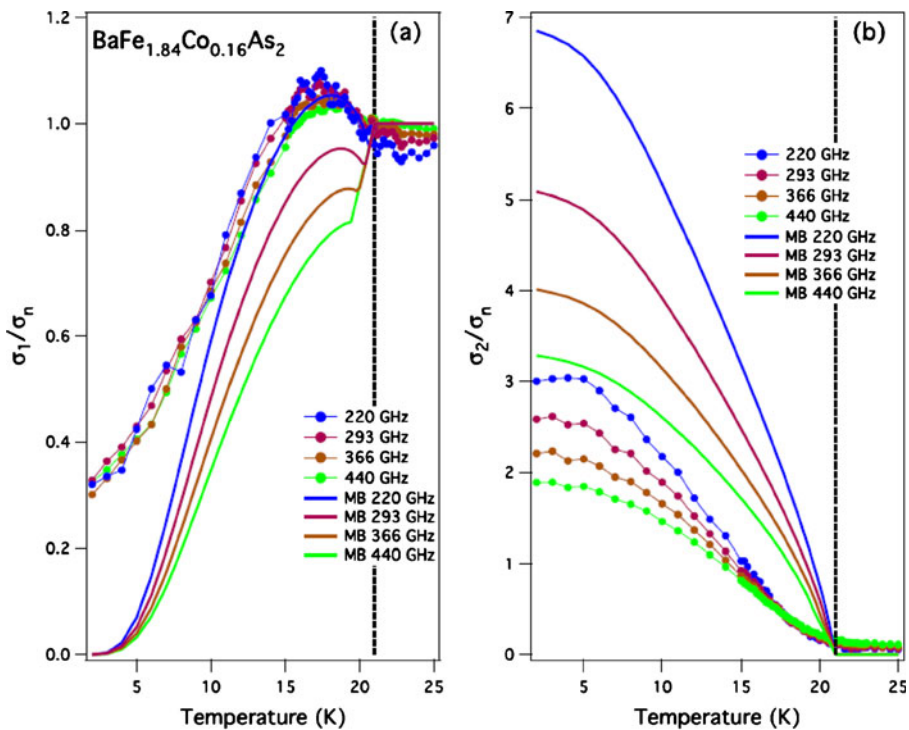


Fig. 30 Normalised **a** σ_1 and **b** σ_2 for $\text{BaFe}_{1.84}\text{Co}_{0.16}\text{As}_2$ thin films (points) at various frequencies, compared with Mattis–Bardeen theory (solid lines) [206]. Reproduced with permission from Ref. [206]. Copyright © 2010, American Physical Society.

ratio T_s/T_n between superconducting and normal states was observed to drop dramatically over the course of 1 ps for photon energies above the superconducting gap energy (2.8 meV), and to not recover within the 6 ps time window. The estimated electron temperature induced by the visible pulse was 30K–50K, well above T_c . The first study to directly observe the recovery of the superconducting condensate was by Kaindl *et al.* [209], who use the two-fluid model to simulate the time-resolved conductivity change of $\text{Bi}_2\text{Sr}_2\text{CaCu}_2\text{O}_8 + \delta$ following the condensate’s destruction with a 1.55 eV pulse, and subsequent recovery over 50 ps (Fig. 31).

7.2 Other strongly correlated systems

The application of a magnetic field causes some materials to exhibit a dramatic change in electrical resistance, often orders of magnitude in amplitude, termed colossal magnetoresistance (CMR). Averitt *et al.* [210] used THz-TDS to examine the equilibrium and photoconductivity of the transition metal manganites $\text{La}_{0.7}\text{Ca}_{0.3}\text{MnO}_3$ and $\text{La}_{0.7}\text{Sr}_{0.3}\text{MnO}_3$ thin films, with ordering temperatures of 250 K and 360 K respectively. The dynamics of the time-resolved suppression in the conductivity after photoexcitation was modeled

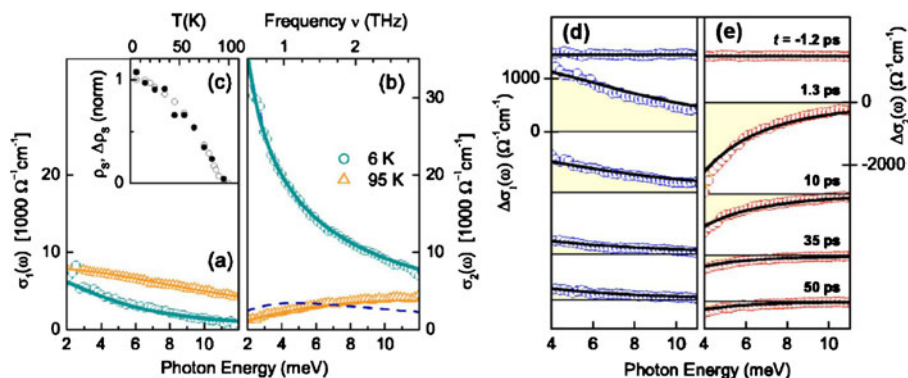
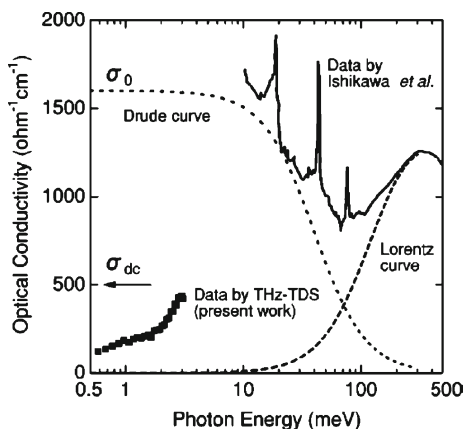


Fig. 31 Photoinduced destruction of Cooper pairs in $\text{Bi}_2\text{Sr}_2\text{CaCu}_2\text{O}_{8+\delta}$ observed in the time-domain. The equilibrium **a** σ_1 and **b** σ_2 of BSCCO does not exhibit a charge gap in the spectral range up to 12 meV (~ 3 THz). *Solid lines* indicate fits using the two-fluid model. Upon photoexcitation **d** σ_1 increases, while **e** σ_2 decreases. The reformation of the superconducting condensate is almost complete within 50 ps. The *inset c* shows how the superfluid density ρ_s and initial photoinduced change in ρ_s vary with temperature [209]. Reproduced with permission from Ref. [209]. Copyright © 2005, American Physical Society.

taking spin-lattice relaxation into account [210]. Takahashi *et al.* [211] identified a pseudogap in the THz conductivity of thin films of magnetoresistive $\text{La}_{2-2x}\text{Sr}_{1+2x}\text{Mn}_2\text{O}_7$ around 2 meV, as indicated by σ_1 in Fig. 32. The importance of this finding was that it ruled out a Drude-like conductivity term for delocalised electrons (dashed line), which a previous FTIR study could not disclude [211]. The temperature and magnetic field dependence of the THz conductivity of the CMR compound $\text{Pr}_{0.65}\text{Ca}_{0.28}\text{Sr}_{0.07}\text{MnO}_3$ was examined by Pimenov *et al.* on the insulating side of the metal-insulator transition [212].

The wide-bandgap insulator $12 \text{ CaO} \cdot 7 \text{ Al}_2\text{O}_3$, which consists of sub-nanometer sized oxide cages, can be made conductive by incorporating hydrogen ions [213]. Harimochi *et al.* reported that the THz conductivity of this system obeyed the Jonscher law $\sigma_1 \propto \omega^s$, with $s = 0.65$ [214], suggesting that the variable-range hopping of localised electrons dominated transport. A

Fig. 32 Real part of conductivity of LSMO obtained from THz-TDS and FTIR. In the THz range the conductivity is gapped [211]. Reproduced with permission from Ref. [211]. Copyright © 2003, American Institute of Physics.

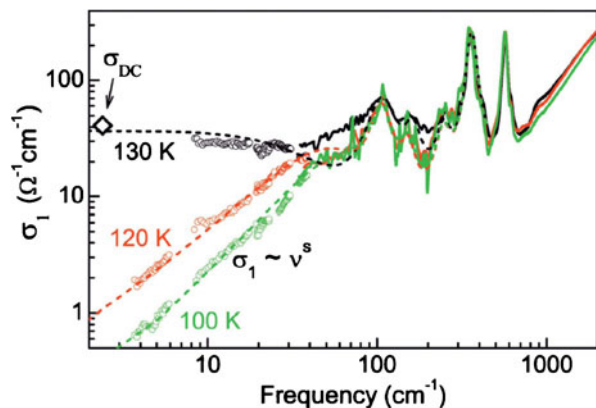


subsequent study extended this work and presented a polaron hopping model [215]. Magnetite (Fe_3O_4) undergoes a metal-insulator transition at ~ 125 K, below which the dc conductivity is reduced by two orders of magnitude. Pimenov *et al.* detailed the THz and infrared conductivity of this important magnetic material [216] using a Mach-Zehnder interferometer and an FTIR, as reproduced in Fig. 33. The frequency dependence of σ_1 was witnessed to obey the Jonscher law below the transition temperature, but to become Drude-like immediately above. The equilibrated photoconductivity of the Mott insulator YTiO_3 was found to also obey the Jonscher expression, with negative imaginary part [217] and photoexcitations that persisted for several milliseconds.

The metal-insulator transition in the compound VO_2 (at 340 K) has been extensively investigated by THz-TDS. The equilibrium THz conductivity was examined by Jepsen *et al.* [218], who reported that the phase transition occurred through the growth of metallic domains in the uniform material. Maxwell–Garnett effective medium theory using the Drude–Lorentz model for the conductive regions allowed their data to be modelled more accurately than Bruggeman EMT. Kubler *et al.* [219] reported that the transition was triggerable on an ultrafast timescale by a 12 fs infrared pulse. This induced a coherent oscillation of V–V dimers at 6 THz, which was visible as an oscillation in $\Delta\sigma_1(E = 60 \text{ meV}, t)$, where t is the pump-probe delay. The THz conductivity of nanoparticles of VO_2 were also investigated [220], and the Drude–Smith model (Eq. 20) with $\tau = 20$ fs and $c_1 = -0.7$ gave good agreement with experiment. While the Bruggeman EMT was reported to give poorer fits, a short lifetime of $\tau = 2$ fs was assumed for the metallic phase.

Transition metal oxides can also exhibit states with novel electric and magnetic order. Below 240 K, charges and spins in the layered nickelate $\text{La}_{2-x}\text{Sr}_x\text{NiO}_{4+\delta}$ (LSNO) order in one-dimensional stripes in the $a-b$ plane [Fig. 34, left], with a pronounced effect on the conductivity at THz frequencies [221]. The conductivity function $\sigma'(\omega) = \omega\epsilon_0(\epsilon - \epsilon_\infty)$ (i.e. including the lattice response, Section 2.1) was reported to exhibit a negative σ'_2 , arising

Fig. 33 The magnetic compound magnetite (Fe_3O_4) undergoes a metal-insulator transition at 125 K that can be readily seen by the THz conductivity. The Jonscher conductivity law for variable-range hopping fits σ_1 (dashed straight lines) [216]. Reproduced with permission from Ref. [216]. Copyright © 2005, American Physical Society.



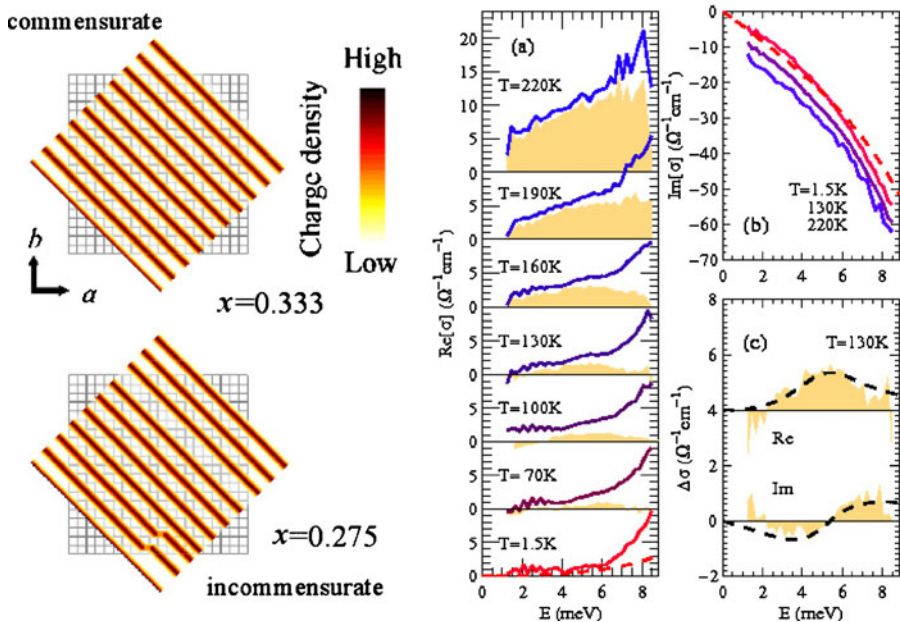


Fig. 34 *Left:* cartoon of $a-b$ plane charge stripe order in commensurate and incommensurate LSNO. **a** At temperatures well below the charge stripe ordering temperature (240 K) σ'_1 of commensurate LSNO is minimal in the range up to 8 meV. *Shaded areas* show the additional conductivity compared with at 1.5 K. **b** σ'_2 at different temperatures (offset) is dominated by a high-lying phonon mode (*dashed line*). **c** In the intermediate temperature range the thermally activated σ' (*shaded*) exhibits a resonance, modelled by the collective mode of a charge density wave (*dashed lines*) [221]. Reproduced with permission from Ref. [221]. Copyright © 2008, American Physical Society.

from a phonon mode above the experimental bandwidth, that was almost independent of temperature (Fig. 34b). By examining the thermally excited conductivity the authors were able to provide evidence for a charge density wave (CDW), a quasi-1D modulation of charge density, pinned by lattice defects (Fig. 34a and c). The optical response of a CDW consists of a gapped conductivity ($2\Delta \sim 0.1$ eV for $\text{La}_{2-x}\text{Sr}_x\text{NiO}_{4+\delta}$) and a lower-energy collective mode within the gap [222]. This collective mode was found to be centred at 5.4 meV when the charge stripes were commensurate with the lattice (Fig. 34c), where this energy corresponds to the pinning energy of the mode. For incommensurate LSNO, where the charge stripe order does not perfectly match the lattice (Fig. 34, left), the mode was more weakly pinned at 3.9 meV.

8 Conclusion

Terahertz radiation, in particular THz time-domain spectroscopy, stands on the cusp of becoming a routine research tool used by scientists in disparate fields. The breadth and depth of the studies of conductive solid state materials

using terahertz radiation continues to advance and to impress. As the field is so broad no single review can hope to discuss all the work published to date. We hope however that the above description of some of the historic and recent contributions will help to inform and guide future research.

Acknowledgements JL would like to acknowledge the EPSRC (UK) for a Fellowship. This work was partially supported by a National Research Foundation of Korea (NRF) grant funded by the Korea government (MEST) (No. 2010-0009070 and No. 2011-0001053).

References

1. B. Ferguson, X.C. Zhang, *Nat. Mater.* **1**, 26 (2002)
2. C.A. Schmuttenmaer, *Chem. Rev.* **104**, 1759 (2004)
3. M. Tonouchi, *Nat. Photon.* **1**, 97 (2007)
4. J.B. Baxter, G.W. Guglietta, *Anal. Chem.* **83**, 4342 (2011)
5. P.U. Jepsen, D.G. Cooke, M. Koch, *Laser Photon. Rev.* **5**, 124 (2011)
6. R. Ulbricht, E. Hendry, J. Shan, T.F. Heinz, M. Bonn, *Rev. Mod. Phys.* **83**, 543 (2011)
7. H. Némec, P. Kužel, V. Sundström, *J. Photochem. Photobiol. A-Chem.* **215**, 123 (2010)
8. R.D. Averitt, A.J. Taylor, *J. Phys. Condens. Matter* **14**, R1357 (2002)
9. D.N. Basov, R.D. Averitt, D. van der Marel, M. Dressel, K. Haule, *Rev. Mod. Phys.* **83**, 471 (2011)
10. A.J.L. Adam, *J Infrared Milli Terahz Waves* **32**, 1 (2011)
11. T. Löffler, M. Kreß, M. Thomson, T. Hahn, N. Hasegawa, H.G. Roskos, *Semicond. Sci. Technol.* **20**, S134 (2005)
12. M.D. Thomson, M. Kreß, T. Löffler, H.G. Roskos, *Laser Photon. Rev.* **1**, 349 (2007)
13. D.H. Auston, *Appl. Phys. Lett.* **26**, 101 (1975)
14. D.H. Auston, K.P. Cheung, P.R. Smith, *Appl. Phys. Lett.* **45**, 284 (1984)
15. X.C. Zhang, B.B. Hu, J.T. Darrow, D.H. Auston, *Appl. Phys. Lett.* **56**, 1011 (1990)
16. M.B. Johnston, D.M. Whittaker, A. Corchia, A.G. Davies, E.H. Linfield, *Phys. Rev. B* **65**, 165301 (2002)
17. G. Klatt, F. Hilser, W. Qiao, M. Beck, R. Gebis, A. Bartels, K. Huska, U. Lemmer, G. Bastian, M.B. Johnston, M. Fischer, J. Faist, T. Dekorsy, *Opt. Express* **18**, 4939 (2010)
18. D.H. Auston, K.P. Cheung, *J. Opt. Soc. Am. B, Opt. Phys.* **2**, 606 (1985)
19. P.C.M. Planken, H.K. Nienhuys, H.J. Bakker, T. Wenckebach, *J. Opt. Soc. Am. B, Opt. Phys.* **18**, 313 (2001)
20. G. Zhao, R.N. Schouten, W.T. Wenckebach, P.C.M. Planken, *Rev. Sci. Instrum.* **73**, 1715 (2002)
21. E. Castro-Camus, L. Fu, J. Lloyd-Hughes, H.H. Tan, C. Jagadish, M.B. Johnston, *J. Appl. Phys.* **104**, 053113 (2008)
22. S. Nashima, O. Morikawa, K. Takata, M. Hangyo, *Appl. Phys. Lett.* **79**, 3923 (2001)
23. A. Pashkin, M. Kempa, H. Némec, F. Kadlec, P. Kužel, *Rev. Sci. Instrum.* **74**, 4711 (2003)
24. P.U. Jepsen, B.M. Fischer, *Opt. Lett.* **30**, 29 (2005)
25. L. Duvillearet, F. Garet, J.L. Coutaz, *IEEE J. Sel. Top. Quantum Electron.* **2**, 739 (1996)
26. R.E.G. III, M. Tinkham, *Phys. Rev.* **108**, 243 (1957)
27. H.K. Nienhuys, V. Sundström, *Appl. Phys. Lett.* **87**, 012101 (2005)
28. P. Parkinson, J. Lloyd-Hughes, Q. Gao, H.H. Tan, C. Jagadish, M.B. Johnston, L.M. Herz, *Nano Lett.* **7**, 2162 (2007)
29. J.M. Pitarke, V.M. Silkin, E.V. Chulkov, P.M. Echenique, *Rep. Prog. Phys.* **70**, 1 (2007)
30. N.V. Smith, *Phys. Rev. B* **64**, 155106 (2001)
31. N.F. Mott, M. Kaveh, *Adv. Phys.* **34**, 329 (1985)
32. T.-I. Jeon, D. Grischkowsky, A. Mukherjee, R. Menon, *Appl. Phys. Lett.* **79**, 4142 (2001)
33. T.-I. Jeon, D. Grischkowsky, A. Mukherjee, R. Menon, *Appl. Phys. Lett.* **81**, 2902 (2002)
34. K.H. Lee, A.J. Heeger, Y. Cao, *Phys. Rev. B* **48**, 14884 (1993)
35. G. Grosso, G. Parravicini, *Solid State Physics* (Academic Press, 2000)

36. P.Y. Yu, M. Cardona, *Fundamentals of Semiconductors*, 3rd edn. (Springer, 2003)
37. J. Lloyd-Hughes, Appl. Phys. Lett. **100**, 122103 (2012)
38. T. Unuma, M. Yoshita, T. Noda, H. Sakaki, H. Akiyama, J. Appl. Phys. **93**, 1586 (2003)
39. T.-I. Jeon, D. Grischkowsky, Phys. Rev. Lett. **78**, 1106 (1997)
40. T. Ando, Z. Physik B **24**, 33 (1976)
41. R.H.M. Groeneveld, D. Grischkowsky, J. Opt. Soc. Am. B, Opt. Phys. **11**, 2502 (1994)
42. R.A. Kaindl, M.A. Carnahan, D. Hägele, R. Lövenich, D.S. Chemla, Nature **423**, 734 (2003)
43. R. Huber, R.A. Kaindl, B.A. Schmid, D.S. Chemla, Phys. Rev. B **72**, 161314 (2005)
44. R.A. Kaindl, D. Hägele, M.A. Carnahan, D.S. Chemla, Phys. Rev. B **79**, 045320 (2009)
45. D.C. Mattis, J. Bardeen, Phys. Rev. **111**, 412 (1958)
46. A.J. Berlinsky, C. Kallin, G. Rose, A.C. Shi, Phys. Rev. B **48**, 4074 (1993)
47. S.D. Brorson, R. Buhleier, I.E. Trofimov, J.O. White, C. Ludwig, F.F. Balakirev, H.U. Haberman, J. Kuhl, J. Opt. Soc. Am. B, Opt. Phys. **13**, 1979 (1996)
48. W. Gotze, P. Wolfle, Phys. Rev. B **6**, 1226 (1972)
49. D.N. Basov, T. Timusk, Rev. Mod. Phys. **77**, 721 (2005)
50. E. Hendry, M. Koeberg, B. O'Regan, M. Bonn, Nano Lett. **6**, 755 (2006)
51. D. Polder, J. van Santen, Physica **12**, 257 (1946)
52. D.A.G. Bruggeman, Ann. Physik **416**, 636 (1935)
53. M. Scheller, S. Wietzke, C. Jansen, M. Koch, J. Phys. D, Appl. Phys. **42**, 065415 (2009)
54. J.C. Dyre, J. Appl. Phys. **64**, 2456 (1988)
55. J.C. Dyre, Phys. Rev. B **48**, 12511 (1993)
56. K. Shimakawa, H. Naito, S.O. Kasap, Philos. Mag. Lett. **89**, 673 (2009)
57. K. Shimakawa, T. Itoh, H. Naito, S.O. Kasap, Appl. Phys. Lett. **100**, 132102 (2012)
58. D.G. Cooke, A.N. MacDonald, A. Hryciw, J. Wang, Q. Li, A. Meldrum, F.A. Hegmann, Phys. Rev. B **73**, 193311 (2006)
59. B.K. Ridley, *Quantum Processes in Semiconductors*, 4th edn. (Oxford University Press, 2004)
60. J. Lloyd-Hughes, E. Castro-Camus, M.D. Fraser, C. Jagadish, M.B. Johnston, Phys. Rev. B **70**, 235330 (2004)
61. D.S. Kim, D.S. Citrin, Appl. Phys. Lett. **87**, 061108 (2005)
62. E. Castro-Camus, J. Lloyd-Hughes, M.B. Johnston, Phys. Rev. B **71**, 195301 (2005)
63. J. Lloyd-Hughes, E. Castro-Camus, M.B. Johnston, Solid State Commun. **136**, 595 (2005)
64. D.S. Kim, D.S. Citrin, Appl. Phys. Lett. **88**, 161117 (2006)
65. K.J. Willis, S.C. Hagness, I. Knezevic, Appl. Phys. Lett. **96**, 062106 (2010)
66. H. Němec, P. Kužel, V. Sundström, Phys. Rev. B **79**, 115309 (2009)
67. H. Němec, P. Kužel, F. Kadlec, D. Fattakhova-rohlifing, J. Szeifert, T. Bein, V. Kalousek, J. Rathousky, Appl. Phys. Lett. **96**, 062103 (2010)
68. R. Kubo, J. Phys. Soc. Jpn. **12**, 570 (1957)
69. P. Prins, F.C. Grozema, J.M. Schins, S. Patil, U. Scherf, L.D.A. Siebbeles, Phys. Rev. Lett. **96**, 146601 (2006)
70. Z. Mics, H. Němec, I. Rychetsky, P. Kužel, P. Formanek, P. Maly, P. Nemeč, Phys. Rev. B **83**, 155326 (2011)
71. D. Grischkowsky, S. Keiding, M. van Exter, C. Fattinger, J. Opt. Soc. Am. B, Opt. Phys. **7**, 2006 (1990)
72. M. van Exter, D. Grischkowsky, Phys. Rev. B **41**, 12140 (1990)
73. T.-I. Jeon, D. Grischkowsky, Appl. Phys. Lett. **72**, 2259 (1998)
74. S. Nashima, O. Morikawa, K. Takata, M. Hangyo, J. Appl. Phys. **90**, 837 (2001)
75. T.-I. Jeon, D. Grischkowsky, Appl. Phys. Lett. **72**, 3032 (1998)
76. M. Herrmann, M. Tani, K. Sakai, R. Fukasawa, J. Appl. Phys. **91**, 1247 (2002)
77. N. Katzenellenbogen, D. Grischkowsky, Appl. Phys. Lett. **61**, 840 (1992)
78. P.G. Huggard, J.A. Cluff, G.P. Moore, C.J. Shaw, S.R. Andrews, S.R. Keiding, E.H. Linfield, D.A. Ritchie, J. Appl. Phys. **87**, 2382 (2000)
79. M.C. Nuss, D.H. Auston, F. Capasso, Phys. Rev. Lett. **58**, 2355 (1987)
80. B.I. Greene, J.F. Federici, D.R. Dykaar, A.F.J. Levi, L. Pfeiffer, Opt. Lett. **16**, 48 (1991)
81. P.N. Saeta, J.F. Federici, B.I. Greene, D.R. Dykaar, Appl. Phys. Lett. **60**, 1477 (1992)
82. S.E. Ralph, Y. Chen, J. Woodall, D. McInturff, Phys. Rev. B **54**, 5568 (1996)
83. S.S. Prabhu, S.E. Ralph, M.R. Melloch, E.S. Harmon, Appl. Phys. Lett. **70**, 2419 (1997)
84. B.N. Flanders, D.C. Arnett, N.F. Scherer, IEEE J. Sel. Top. Quantum Electron. **4**, 353 (1998)
85. M.C. Beard, G.M. Turner, C.A. Schmuttenmaer, Phys. Rev. B **62**, 15764 (2000)

86. M.C. Beard, G.M. Turner, C.A. Schmuttenmaer, *J. Appl. Phys.* **90**, 5915 (2001)
87. M.C. Beard, C.A. Schmuttenmaer, *J. Chem. Phys.* **114**, 2903 (2001)
88. R. Huber, F. Tauser, A. Brodschelm, M. Bichler, G. Abstreiter, A. Leitenstorfer, *Nature* **414**, 286 (2001)
89. R. Huber, C. Kübler, S. Tubel, A. Leitenstorfer, Q.T. Vu, H. Haug, F. Kohler, M.C. Amann, *Phys. Rev. Lett.* **94**, 027401 (2005)
90. D.M. Mittleman, J. Cunningham, M.C. Nuss, M. Geva, *Appl. Phys. Lett.* **71**, 16 (1997)
91. K. Yatsugi, N. Matsumoto, T. Nagashima, M. Hangyo, *Appl. Phys. Lett.* **98**, 212108 (2011)
92. W. Zhang, A.K. Azad, D. Grischkowsky, *Appl. Phys. Lett.* **82**, 2841 (2003)
93. G.H. Ma, D. Li, H. Ma, J. Shen, C.G. Wu, J. Ge, S.H. Hu, N. Dai, *Appl. Phys. Lett.* **93**, 211101 (2008)
94. J.B. Baxter, C.A. Schmuttenmaer, *Phys. Rev. B* **80**, 235205 (2009)
95. X.H. Zhang, H.C. Guo, A.M. Yong, J.D. Ye, S.T. Tan, X.W. Sun, *J. Appl. Phys.* **107**, 033101 (2010)
96. T.T. Kang, M. Yamamoto, M. Tanaka, A. Hashimoto, A. Yamamoto, R. Sudo, A. Noda, D.W. Liu, K. Yamamoto, *Opt. Lett.* **34**, 2507 (2009)
97. A. Schneider, *Opt. Lett.* **35**, 265 (2010)
98. T.T. Kang, M. Yamamoto, M. Tanaka, A. Hashimoto, A. Yamamoto, R. Suto, A. Noda, D.W. Liu, K. Yamamoto, *Opt. Lett.* **35**, 266 (2010)
99. J. Lloyd-Hughes, S.K.E. Merchant, L. Fu, H.H. Tan, C. Jagadish, E. Castro-Camus, M.B. Johnston, *Appl. Phys. Lett.* **89**, 232102 (2006)
100. G.M. Turner, M.C. Beard, C.A. Schmuttenmaer, *J. Phys. Chem. B* **106**, 11716 (2002)
101. P. Tiwana, P. Parkinson, M.B. Johnston, H.J. Snaith, L.M. Herz, *J. Phys. Chem. C* **114**, 1365 (2010)
102. P. Tiwana, P. Docampo, M.B. Johnston, H.J. Snaith, L.M. Herz, *ACS Nano* **5**, 5158 (2011)
103. E. Hendry, F. Wang, J. Shan, T.F. Heinz, M. Bonn, *Phys. Rev. B* **69**, 081101 (2004)
104. L.V. Titova, T.L. Cocker, D.G. Cooke, X.Y. Wang, A. Meldrum, F.A. Hegmann, *Phys. Rev. B* **83**, 085403 (2011)
105. P. Parkinson, H.J. Joyce, Q. Gao, H.H. Tan, X. Zhang, J. Zou, C. Jagadish, L.M. Herz, M.B. Johnston, *Nano Lett.* **9**, 3349 (2009)
106. H. Němec, J. Rochford, O. Taratula, E. Galoppini, P. Kužel, T. Polívka, A. Yartsev, V. Sundström, *Phys. Rev. Lett.* **104**, 197401 (2010)
107. S. Ramani, A. Cheville, J.E. Garcia, V. Agarwal, *Phys. Status Solidi C* **4**, 2111 (2007)
108. S.K.E. Merchant, J. Lloyd-Hughes, L. Sirbu, I.M. Tiginyanu, P. Parkinson, L.M. Herz, M.B. Johnston, *Nanotechnology* **19**, 395704 (2008)
109. J. Lloyd-Hughes, S. Mueller, G. Scalari, H. Bishop, A. Crossley, M. Enachi, L. Sirbu, I.M. Tiginyanu, *Appl. Phys. Lett.* **100**, 132106 (2012)
110. J. Lloyd-Hughes, S.K.E. Merchant, L. Sirbu, I.M. Tiginyanu, M.B. Johnston, *Phys. Rev. B* **78**, 085320 (2008)
111. N.A. Kabir, Y. Yoon, J.R. Knab, J.Y. Chen, A.G. Markelz, J.L. Reno, Y. Sadofyev, S. Johnson, Y.H. Zhang, J.P. Bird, *Appl. Phys. Lett.* **89**, 132109 (2006)
112. J. Lloyd-Hughes, Y.L. Delley, G. Scalari, M. Fischer, V. Liverini, M. Beck, J. Faist, *J. Appl. Phys.* **106**, 093104 (2009)
113. R. Kohler, A. Tredicucci, F. Beltram, H.E. Beere, E.H. Linfield, A.G. Davies, D.A. Ritchie, R.C. Iotti, F. Rossi, *Nature* **417**, 156 (2002)
114. G. Scalari, C. Walthers, M. Fischer, R. Terazzi, H. Beere, D. Ritchie, J. Faist, *Laser Photon. Rev.* **3**, 45 (2009)
115. P.G. Huggard, J.A. Cluff, C.J. Shaw, S.R. Andrews, E.H. Linfield, D.A. Ritchie, *Appl. Phys. Lett.* **71**, 2647 (1997)
116. X.F. Wang, D.J. Hilton, L. Ren, D.M. Mittleman, J. Kono, J.L. Reno, *Opt. Lett.* **32**, 1845 (2007)
117. J. Lloyd-Hughes, H.E. Beere, D.A. Ritchie, M.B. Johnston, *Phys. Rev. B* **77**, 125322 (2008)
118. G. Scalari, C. Maissen, D. Turčinková, D. Hagenmüller, de Liberato, C. Ciuti, C. Reichl, D. Schuh, W. Wegscheider, M. Beck, J. Faist, *Science* **335**, 1323 (2012)
119. J. Kröll, J. Darms, S.S. Dhillon, X. Marcadet, M. Calligaro, C. Sirtori, K. Unterrainer, *Nature* **449**, 698 (2007)
120. W. Parz, T. Müller, J. Darms, K. Unterrainer, M. Austerer, G. Strasser, L.R. Wilson, J.W. Cockburn, A.B. Krysa, J.S. Roberts, *Appl. Phys. Lett.* **93**, 091105 (2008)

121. N. Jukam, S.S. Dhillon, D. Oustinov, Z. Zhao, S. Hameau, J. Tignon, S. Barbieri, A. Vasanelli, P. Filloux, C. Sirtori, X. Marcadet, *Appl. Phys. Lett.* **93**, 101115 (2008)
122. N. Jukam, S.S. Dhillon, D. Oustinov, J. Madeo, C. Manquest, S. Barbieri, C. Sirtori, S.P. Khanna, E.H. Linfield, A.G. Davies, J. Tignon, *Nat. Photonics* **3**, 715 (2009)
123. J. Lloyd-Hughes, G. Scalari, A. van Kolck, M. Fischer, M. Beck, J. Faist, *Opt. Express* **17**, 18387 (2009)
124. G. Gunter, A.A. Anappara, J. Hees, A. Sell, G. Biasiol, L. Sorba, C. Ciuti, A. Tredicucci, A. Leitenstorfer, R. Huber, *Nature* **458**, 178 (2009)
125. M.C. Beard, G.M. Turner, J.E. Murphy, O.I. Mičić, M.C. Hanna, A.J. Nozik, C.A. Schmuttenmaer, *Nano Lett.* **3**, 1695 (2003)
126. M.C. Beard, G.M. Turner, C.A. Schmuttenmaer, *Nano Lett.* **2**, 983 (2002)
127. F. Wang, J. Shan, M.A. Islam, I.P. Herman, M. Bonn, T.F. Heinz, *Nat. Mater.* **5**, 861 (2006)
128. E. Hendry, M. Koeberg, F. Wang, H. Zhang, C.D. Donega, D. Vanmaekelbergh, M. Bonn, *Phys. Rev. Lett.* **96**, 057408 (2006)
129. D.A. Yarotski, R.D. Averitt, N. Negre, S.A. Crooker, A.J. Taylor, G.P. Donati, A. Stintz, L.F. Lester, K.J. Malloy, *J. Opt. Soc. Am. B, Opt. Phys.* **19**, 1480 (2002)
130. D.G. Cooke, F.A. Hegmann, Y.I. Mazur, W.Q. Ma, X. Wang, Z.M. Wang, G.J. Salamo, M. Xiao, T.D. Mishima, M.B. Johnson, *Appl. Phys. Lett.* **85**, 3839 (2004)
131. R.P. Prasankumar, A. Scopatz, D.J. Hilton, A.J. Taylor, R.D. Averitt, J.M. Zide, A.C. Gossard, *Appl. Phys. Lett.* **86**, 201107 (2005)
132. T. Müller, W. Parz, K. Unterrainer, S. Sauvage, J. Houel, P. Boucaud, A. Miard, A. Lemaître, *Phys. Rev. B* **77**, 035314 (2008)
133. H.P. Porte, P.U. Jepsen, N. Daghestani, E.U. Rafailov, D. Turchinovich, *Appl. Phys. Lett.* **94**, 262104 (2009)
134. D.G. Cooke, F.A. Hegmann, Y.I. Mazur, Z.M. Wang, W. Black, H. Wen, G.J. Salamo, T.D. Mishima, G.D. Lian, M.B. Johnson, *J. Appl. Phys.* **103**, 023710 (2008)
135. D. Stehr, C.M. Morris, D. Talbayev, M. Wagner, H.C. Kim, A.J. Taylor, H. Schneider, P.M. Petroff, M.S. Sherwin, *Appl. Phys. Lett.* **95**, 251105 (2009)
136. A.K. Geim, P. Kim, *Scientific American*, p. 90 (2008)
137. Y.M. Lin, K.A. Jenkins, A. Valdes-garcia, J.P. Small, D.B. Farmer, P. Avouris, *Nano Lett.* **9**, 422 (2009)
138. V. Ryzhii, M. Ryzhii, T. Otsuji, *J. Appl. Phys.* **101**, 083114 (2007)
139. F. Rana, *IEEE Trans. Nanotech.* **7**, 91 (2008)
140. N.L. Rangel, J.M. Seminario, *J. Phys. Chem. A* **112**, 13699 (2008)
141. N.L. Rangel, J.M. Seminario, *J. Chem. Phys.* **132**, 125102 (2010)
142. T. Otsuji, T. Watanabe, H. Karasawa, T. Komori, A. Satou, T. Suemitsu, M. Suemitsu, E. Sano, W. Knap, V. Ryzhii, *J. Infrared Millim. Terahertz Waves* **32**, 629 (2011)
143. P.A. George, J. Strait, J. Dawlaty, S. Shivaraman, M. Chandrashekhar, F. Rana, M.G. Spencer, *Nano Lett.* **8**, 4248 (2008)
144. J.M. Dawlaty, S. Shivaraman, J. Strait, P. George, M. Chandrashekhar, F. Rana, M.G. Spencer, D. Veksler, Y.Q. Chen, *Appl. Phys. Lett.* **93**, 131905 (2008)
145. D. Sun, Z.K. Wu, C. Divin, X.B. Li, C. Berger, P.N. First, T.B. Norris, *Phys. Rev. Lett.* **101**, 157402 (2008)
146. H. Choi, F. Borondics, D.A. Siegel, S.Y. Zhou, M.C. Martin, A. Lanzara, R.A. Kaindl, *Appl. Phys. Lett.* **94**, 172102 (2009)
147. T. Hofmann, A. Boosalis, P. Kuhne, C.M. Herzinger, J.A. Woollam, D.K. Gaskill, J.L. Tedesco, M. Schubert, *Appl. Phys. Lett.* **98**, 041906 (2011)
148. J.L. Tomaino, A.D. Jameson, J.W. Kevek, M.J. Paul, A.M. v d Zande, R.A. Barton, P.L. McEuen, E.D. Minot, Y. Lee, *Opt. Express* **19**, 141 (2011)
149. A.R. Wright, X.G. Xu, J.C. Cao, C. Zhang, *Appl. Phys. Lett.* **95**, 072101 (2009)
150. N. Hamada, S. Sawada, A. Oshiyama, *Phys. Rev. Lett.* **68**, 1579 (1992)
151. O. Hilt, H.B. Brom, M. Ahlskog, *Phys. Rev. B* **61**, R5129 (2000)
152. P.W. Barone, S. Baik, D.A. Heller, M. Strano, *Nat. Mater.* **4**, 86 (2005)
153. M.E. Itkis, F. Borondics, A. Yu, R.C. Haddon, *Science* **312**, 413 (2006)
154. Y. Kawano, T. Uchida, K. Ishibashi, *Appl. Phys. Lett.* **95**, 083123 (2009)
155. T.-I. Jeon, K.J. Kim, C. Kang, S.J. Oh, J.H. Son, K.H. An, D.J. Bae, Y.H. Lee, *Appl. Phys. Lett.* **80**, 3403 (2002)

156. L. Ren, C.L. Pint, L.G. Booshenri, W.D. Rice, X.F. Wang, D.J. Hilton, K. Takeya, I. Kawayama, M. Tonouchi, R.H. Hauge, J. Kono, *Nano Lett.* **9**, 2610 (2009)
157. A. Ugawa, A.G. Rinzier, D.B. Tanner, *Phys. Rev. B* **60**, R11305 (1999)
158. T.-I. Jeon, K.J. Kim, C. Kang, I.H. Maeng, J.H. Son, K.H. An, J.Y. Lee, Y.H. Lee, *J. Appl. Phys.* **95**, 5736 (2004)
159. J. Han, Z. Zhu, Y. Liao, Z. Wang, L. Yu, W. Zhang, L. Sun, T. Wang, *Jetp Lett.* **78**, 436 (2003)
160. T.-I. Jeon, J.H. Son, K.H. An, Y.H. Lee, Y.S. Lee, *J. Appl. Phys.* **98**, 034316 (2005)
161. H. Nishimura, N. Minami, R. Shimano, *Appl. Phys. Lett.* **91**, 011108 (2007)
162. I. Maeng, C. Kang, S.J. Oh, J.H. Son, K.H. An, Y.H. Lee, *Appl. Phys. Lett.* **90**, 051914 (2007)
163. G.Y. Slepyan, M.V. Shuba, S.A. Maksimenko, C. Thomsen, A. Lakhtakia, *Phys. Rev. B* **81**, 205423 (2010)
164. T. Kampfrath, K. v. Volkman, C.M. Aguirre, P. Desjardins, R. Martel, M. Krenz, C. Frischkorn, M. Wolf, L. Perfetti, *Phys. Rev. Lett.* **101**, 267403 (2008)
165. L. Perfetti, T. Kampfrath, F. Schapper, A. Hagen, T. Hertel, C.M. Aguirre, P. Desjardins, R. Martel, C. Frischkorn, M. Wolf, *Phys. Rev. Lett.* **96**, 027401 (2006)
166. X. Xu, K. Chuang, R.J. Nicholas, M.B. Johnston, L.M. Herz, *J. Phys. Chem. C* **113**, 18106 (2009)
167. X.L. Xu, P. Parkinson, K.C. Chuang, M.B. Johnston, R.J. Nicholas, L.M. Herz, *Phys. Rev. B* **82**, 085441 (2010)
168. J.G. Wang, M.W. Graham, Y.Z. Ma, G.R. Fleming, R.A. Kaindl, *Phys. Rev. Lett.* **104**, 177401 (2010)
169. R. Rungsawang, V.G. Geethamma, E.P.J. Parrott, D.A. Ritchie, E.M. Terentjev, *J. Appl. Phys.* **103**, 123503 (2008)
170. G.B. Jung, Y. Myung, Y.J. Cho, Y.J. Sohn, D.M. Jang, H.S. Kim, C.W. Lee, J. Park, I. Maeng, J.H. Son, C. Kang, *J. Phys. Chem. C* **114**, 11258 (2010)
171. J. Kyoung, E.Y. Jang, M.D. Lima, H.R. Park, R.O. Robles, X. Lepro, Y.H. Kim, R.H. Baughman, D.S. Kim, *Nano Lett.* **11**, 4227 (2011)
172. T.-I. Jeon, D. Grischkowsky, A. Mukherjee, R. Menon, *Appl. Phys. Lett.* **77**, 2452 (2000)
173. T.-I. Jeon, D. Grischkowsky, A. Mukherjee, R. Menon, *Synth. Met.* **135**, 451 (2003)
174. T. Unuma, K. Fujii, H. Kishida, A. Nakamura, *Appl. Phys. Lett.* **97**, 033308 (2010)
175. J.L. Brédas, G.B. Street, *Accounts Chem. Res.* **18**, 309 (1985)
176. E. Hendry, J.M. Schins, L.P. Candeias, L.D.A. Siebbeles, M. Bonn, *Phys. Rev. Lett.* **92**, 196601 (2004)
177. E. Hendry, M. Koeberg, J.M. Schins, H.K. Nienhuys, V. Sundström, L.D.A. Siebbeles, M. Bonn, *Phys. Rev. B* **71**, 125201 (2005)
178. E. Hendry, M. Koeberg, J.M. Schins, L.D.A. Siebbeles, M. Bonn, *Chem. Phys. Lett.* **432**, 441 (2006)
179. P. Prins, F.C. Grozema, J.M. Schins, T.J. Savenije, S. Patil, U. Scherf, L.D.A. Siebbeles, *Phys. Rev. B* **73**, 045204 (2006)
180. H. Sirringhaus, *Adv. Mater.* **17**, 2411 (2005)
181. J. Lloyd-Hughes, T. Richards, H. Sirringhaus, E. Castro-Camus, L.M. Herz, M.B. Johnston, *Appl. Phys. Lett.* **89**, 112101 (2006)
182. J. Lloyd-Hughes, T. Richards, H. Sirringhaus, M.B. Johnston, L.M. Herz, *Phys. Rev. B* **77**, 125203 (2008)
183. X. Ai, M.C. Beard, K.P. Knutsen, S.E. Shaheen, G. Rumbles, R.J. Ellingson, *J. Phys. Chem. B* **110**, 25462 (2006)
184. P. Parkinson, J. Lloyd-Hughes, M.B. Johnston, L.M. Herz, *Phys. Rev. B* **78**, 115321 (2008)
185. P.D. Cunningham, L.M. Hayden, *J. Phys. Chem. C* **112**, 7928 (2008)
186. H. Némec, H.K. Nienhuys, F. Zhang, O. Inganäs, A. Yartsev, V. Sundström, *J. Phys. Chem. C* **112**, 6558 (2008)
187. D.G. Cooke, F.C. Krebs, P.U. Jepsen, *Phys. Rev. Lett.* **108**, 056603 (2012)
188. F.A. Hegmann, R.R. Tykwinski, K.P.H. Lui, J.E. Bullock, J.E. Anthony, *Phys. Rev. Lett.* **89**, 227403 (2002)
189. O. Ostroverkhova, D.G. Cooke, S. Shcherbyna, R.F. Egerton, F.A. Hegmann, R.R. Tykwinski, J.E. Anthony, *Phys. Rev. B* **71**, 035204 (2005)
190. O. Ostroverkhova, S. Shcherbyna, D.G. Cooke, R.F. Egerton, F.A. Hegmann, R.R. Tykwinski, S.R. Parkin, J.E. Anthony, *J. Appl. Phys.* **98**, 033701 (2005)

191. O. Ostroverkhova, D.G. Cooke, F.A. Hegmann, J.E. Anthony, V. Podzorov, M.E. Gershenson, O.D. Jurchescu, T.T.M. Palstra, *Appl. Phys. Lett.* **88**, 162101 (2006)
192. O. Ostroverkhova, D.G. Cooke, F.A. Hegmann, R.R. Tykwinski, S.R. Parkin, J.E. Anthony, *Appl. Phys. Lett.* **89**, 192113 (2006)
193. N. Laman, D. Grischkowsky, *Appl. Phys. Lett.* **93**, 051105 (2008)
194. M. Walther, D.G. Cooke, C. Sherstan, M. Hajar, M.R. Freeman, F.A. Hegmann, *Phys. Rev. B* **76**, 125408 (2007)
195. D.R. Lide, *CRC Handbook of Chemistry and Physics*, 73rd edn (1992)
196. A. Thoman, A. Kern, H. Helm, M. Walther, *Phys. Rev. B* **77**, 195405 (2008)
197. L.H. Palmer, M. Tinkham, *Phys. Rev.* **165**, 588 (1968)
198. G.J. Dick, F. Reif, *Phys. Rev.* **181**, 774 (1969)
199. M.C. Nuss, K.W. Goossen, J.P. Gordon, P.M. Mankiewich, M.L. O'Malley, M. Bhushan, J. *Appl. Phys.* **70**, 2238 (1991)
200. S. Spielman, B. Parks, J. Orenstein, D.T. Nemeth, F. Ludwig, J. Clarke, P. Merchant, D.J. Lew, *Phys. Rev. Lett.* **73**, 1537 (1994)
201. B. Parks, S. Spielman, J. Orenstein, D.T. Nemeth, F. Ludwig, J. Clarke, P. Merchant, D.J. Lew, *Phys. Rev. Lett.* **74**, 3265 (1995)
202. F. Gao, J.F. Whitaker, Y. Liu, C. Uher, C.E. Platt, M.V. Klein, *Phys. Rev. B* **52**, 3607 (1995)
203. M. Tinkham, *Introduction to Superconductivity* (McGraw-Hill, 1975)
204. T.R. Tsai, C.C. Chi, S.F. Horng, *Physica C* **391**, 281 (2003)
205. R.A. Kaindl, M.A. Carnahan, J. Orenstein, D.S. Chemla, H.M. Christen, H.Y. Zhai, M. Paranthaman, D.H. Lowndes, *Phys. Rev. Lett.* **88**, 027003 (2002)
206. R.V. Aguilar, L.S. Bilbro, S. Lee, C.W. Bark, J. Jiang, J.D. Weiss, E.E. Hellstrom, D.C. Larbalestier, C.B. Eom, N.P. Armitage, *Phys. Rev. B* **82**, 180514 (2010)
207. T. Fischer, A.V. Pronin, J. Wosnitza, K. Iida, F. Kurth, S. Haindl, L. Schultz, B. Holzapfel, E. Schachinger, *Phys. Rev. B* **82**, 224507 (2010)
208. J.F. Federici, B.I. Greene, P.N. Saeta, D.R. Dykaar, F. Sharifi, R.C. Dynes, *Phys. Rev. B* **46**, 11153 (1992)
209. R.A. Kaindl, M.A. Carnahan, D.S. Chemla, S. Oh, J.N. Eckstein, *Phys. Rev. B* **72**, 060510 (2005)
210. R.D. Averitt, A.I. Lobad, C. Kwon, S.A. Trugman, V.K. Thorsmølle, A.J. Taylor, *Phys. Rev. Lett.* **87**, 017401 (2001)
211. K. Takahashi, N. Kida, M. Tonouchi, *Appl. Phys. Lett.* **83**, 4303 (2003)
212. A. Pimenov, M. Biberacher, D. Ivannikov, A. Loidl, A.A. Mukhin, Y.G. Goncharov, A.M. Balbashov, *Phys. Rev. B* **73**, 220407 (2006)
213. K. Hayashi, S. Matsuishi, T. Kamiya, M. Hirano, H. Hosono, *Nature* **419**, 462 (2002)
214. H. Harimochi, J. Kitagawa, M. Ishizaka, Y. Kadoya, M. Yamanishi, S. Matsuishi, H. Hosono, *Phys. Rev. B* **70**, 193104 (2004)
215. J. Kitagawa, M. Ishizaka, Y. Kadoya, S. Matsuishi, H. Hosono, *J. Phys. Soc. Jpn.* **75**, 084715 (2006)
216. A. Pimenov, S. Tachos, T. Rudolf, A. Loidl, D. Schrupp, M. Sing, R. Claessen, V.A.M. Brabers, *Phys. Rev. B* **72**, 035131 (2005)
217. J. Kitagawa, Y. Kadoya, M. Tsubota, F. Iga, T. Takabatake, *J. Phys. Condens. Matter* **19**, 406224 (2007)
218. P.U. Jepsen, B.M. Fischer, A. Thoman, H. Helm, J.Y. Suh, R. Lopez, J.R.F. Haglund, *Phys. Rev. B* **74**, 205103 (2006)
219. C. Kübler, H. Ehrke, R. Huber, R. Lopez, A. Halabica, J.R.F. Haglund, A. Leitenstorfer, *Phys. Rev. Lett.* **99**, 116401 (2007)
220. T.L. Cocker, L.V. Titova, S. Fourmaux, H.C. Bandulet, D. Brassard, J.C. Kieffer, F.A. Hegmann, *Appl. Phys. Lett.* **97**, 221905 (2010)
221. J. Lloyd-Hughes, D. Prabhakaran, A.T. Boothroyd, M.B. Johnston, *Phys. Rev. B* **77**, 195114 (2008)
222. G. Gruner, *Rev. Mod. Phys.* **60**, 1129 (1988)